Compressive Strength of Advanced High Strength Cold-Formed Steel Members with Compression Warping Restraint only

Chu Ding[1], Damir Akchurin[2], Yu Xia[3], Hannah B. Blum[4], Zhanjie Li[5], Benjamin W. Schafer[6]

Abstract

This work aims to investigate the compressive strength of cold-formed steel members made from Advanced High strength Steel (AHSS) sheets. An experimental investigation has been conducted with 156 pure compression tests on unbraced AHSS columns. Four parameters are varied in the testing: nominal yield stress (340 MPa to 1200MPa), member length (305 mm to 1219 mm), cross-section types (C and Sigma), and section depth (102 mm and 152 mm). The failure behavior of the longer unbraced length columns with higher strength steel are observed to exhibit buckling mode interactions. The peak loads from the tests are compared to the strength predictions by the Direct Strength Method (DSM) implemented in AISI S100 and AS/NZS 4600. It is found that the current DSM cannot conservatively predict the compressive strength of the longer unbraced AHSS columns tested in this study. Design methods proposed in the literature in addition to careful consideration of the test boundary conditions are explored to recommend extensions to the current DSM to address the observed behavior.

1. Introduction

Advanced High strength Steel (AHSS) is a new family of high strength sheet steel with potential cold-formed steel (CFS) construction applications. Unique engineered microstructures enable AHSS grades to obtain yield stresses that exceed conventional high strength steel. In recent years, AHSSs have experienced accelerating adoption in automotive vehicles as structural components [1]. Leveraging automotive industry experiences working with AHSSs, the cold-formed steel framing industry has pathways to developing new high-performance products and opening new markets to using AHSSs.

The Direct Strength Method (DSM) can be used to predict the buckling strength of CFS members. DSM has been adopted in national design specifications and codes including AISI S100 (2022) [2]

---

[1] Adjunct Assistant Research Scientist, Dept. of Civil and Systems Engineering, Johns Hopkins Univ., Baltimore, MD 21218, United States (corresponding author). ORCID: https://orcid.org/0000-0002-9327-593X. Email: chud@jhu.edu

[2] Graduate Research Assistant, Dept. of Civil and Systems Engineering, Johns Hopkins Univ., Baltimore, MD 21218, United States. ORCID: https://orcid.org/0000-0003-0849-4917. Email: akchurd1@jhu.edu

[3] Assistant Professor, School of Engineering and Technology, China Univ. of Geosciences (Beijing), Beijing 100083, China. ORCID: https:// orcid.org/0000-0002-1529-0552. Email: xiayu@cugb.edu.cn

[4] Associate Professor, Dept. of Civil and Environmental Engineering, Univ. of Wisconsin–Madison, Madison, WI 53715, United States. ORCID: https://orcid .org/0000-0003-4672-0903. Email: hannah.blum@wisc.edu

[5] Associate Professor of Civil Engineering, Dept. of Engineering, SUNY Polytechnic Institute, Utica, NY 13502, United States. ORCID: https://orcid.org/0000 -0002-7259-3664. Email: zhanjie.li@sunypoly.edu

[6] Professor, Dept. of Civil and Systems Engineering, Johns Hopkins Univ., Baltimore, MD 21218, United States. ORCID: https://orcid.org/0000-0002-5375-3511. Email: schafer@jhu.edu

and AS/NZS (4600) [3]. However, the high yield stress of AHSSs can potentially present challenges to the applicability of DSM. There are two main challenges. The first challenge results from potential incompatibility in the slenderness range between AHSS members and the members utilized to calibrate the DSM strength expressions. The test dataset assembled for DSM development [4] consists primarily of experiments conducted on mild steel members. CFS members made from AHSS sheets have significantly higher slenderness than their mild steel counterparts. For example, for the slenderness defined in Eq. (1), changing a column member's material from 345 MPa yield stress mild steel to 1000 MPa martensitic AHSS will cause the slenderness to increase by approximately 70%. The performance of DSM in the slenderness range required by AHSS members has not been thoroughly tested. Experimental research on conventional high-strength steel columns has also shown that the current DSM may fail to produce reliable strength predictions [5–9]. This leads to the second main challenge, the primary observed difficulty in the reliability of the current DSM is due to potential buckling interactions. The biggest strength benefits of adopting AHSS are believed to be achieved in complex CFS cross-sections (e.g., lipped channels with intermediate stiffeners and return lips), which are prone to buckling interactions. However, the DSM is developed from tests of primarily mild steel simple cross-sections.

$$\lambda = \sqrt{F_y/F_{cre}} \qquad \text{Eq. (1)}$$

where λ is slenderness, F_y is yield stress and F_{cre} is critical buckling stress.

Buckling interaction refers to a limit state where multiple fundamental buckling modes participate in the formation of the final failure mechanism, e.g., local buckling weakens the flexural moment of inertia triggering a reduced capacity in global buckling. Based on an extensive database of available tests, the current DSM, as adopted, considers only one type of buckling interaction – local-global buckling interaction, as including local-distortional, distortional-global, and local-distortional-global interactions was found to be overly conservative for available data at the time [4].

However, since this time significant research has been conducted to further explore these potential other interactions, including work on local-distortional buckling interaction [10–14], distortional-global buckling interaction [15] and local-distortional-global buckling interaction [16,17]. The studies have shown that specific scenarios are prone to buckling interactions. High yield stress has been suggested as one such scenario prone to greater elastic buckling interactions A recently published study on AHSS flexural members have found current DSM insufficient for members failing in local-distortional buckling [18]. Failure mechanisms in CFS members are formed by through-plate plastification. For members with higher yield stresses, plastification occurs at larger deformations, which makes elastic buckling interactions more likely to develop – such as secondary bifurcation interaction where one mode develops early and other mode(s) emerge and develop. It is hypothesized that AHSS columns may experience more prominent buckling interactions than mild steel ones due to the AHSS's higher yield stresses.

There are only limited studies on buckling interactions in the context of high slenderness driven by yield stress. Earlier studies on buckling interactions largely focused on high slenderness driven by geometric parameters (e.g., member lengths), where the upper limit of yield stress is around 600 MPa. Additionally, study on sheathed high yield stress lipped channels [19] indicates no significant strength erosion due to new forms of buckling interactions. For these reasons, it is necessary to conduct an experimental study to investigate the strengths of AHSS columns to (1) obtain experimental evidence 2.of potential buckling interaction behaviors of AHSS columns, and to (2) evaluate or improve current DSM's applicability to compression members with high yield stresses.

3. Column testing program

3.1 Test set-up

A testing program was carried out in the Thin-Walled Structures Laboratory at Johns Hopkins University. The test set-up is shown in Fig. 1. The tests were conducted on an MTS uniaxial machine with 445 kN capacity. Loading was applied through the cylinder below the bottom loading platen. The tests adopted "bare end" boundary conditions, where the column specimens were directly bearing on the loading platens. Lateral displacements were restrained by friction between column ends and loading platens. This type of boundary conditions has been used in the an earlier column experimental study with good performance [20,21], where a lacking of tensile warping restraint had only limited effect on peak axial loads.

Several sensors were installed to track displacement. Axial shortening was measured through the crosshead at the hydraulic cylinder. Spring loaded position transducers (PTs) were attached to the flange and web at the mid-span of the test specimens using magnets and steel wire, as shown in Fig. 2. Three PTs installed at the web were responsible for measuring web deformation in potential web local buckling or distortional buckling, while the two PTs at one flange were responsible for capturing the flange deformation in potential distortional buckling.

In addition, a camera was set up in front of the test rig to capture images throughout the entire testing process. Image capturing took place every 10 seconds until the testing was concluded. The images were recorded on the same computer as the sensor test, synchronized based on the recorded time stamp, and converted into time-lapse videos for further analysis.

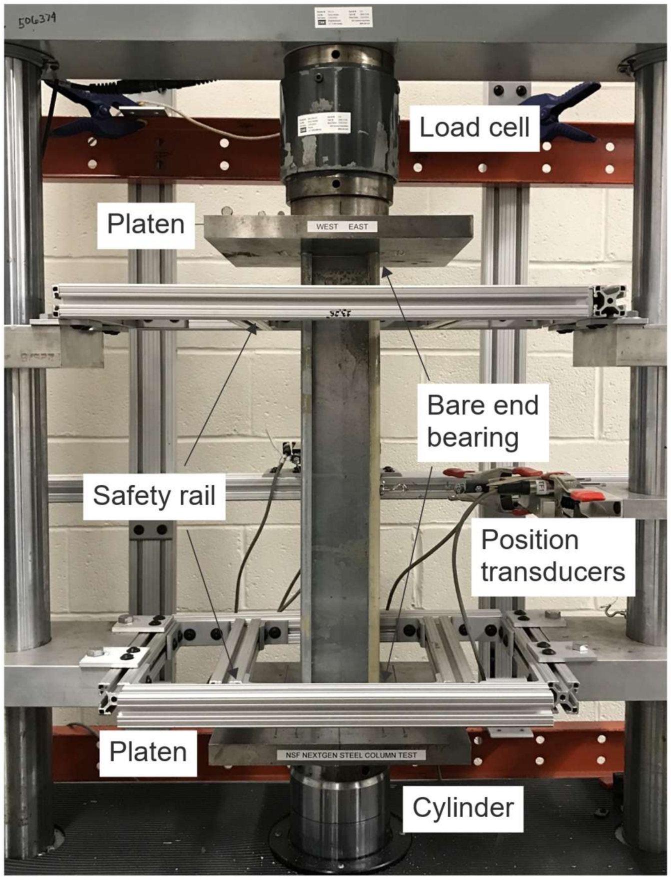

Fig. 1. Test set-up

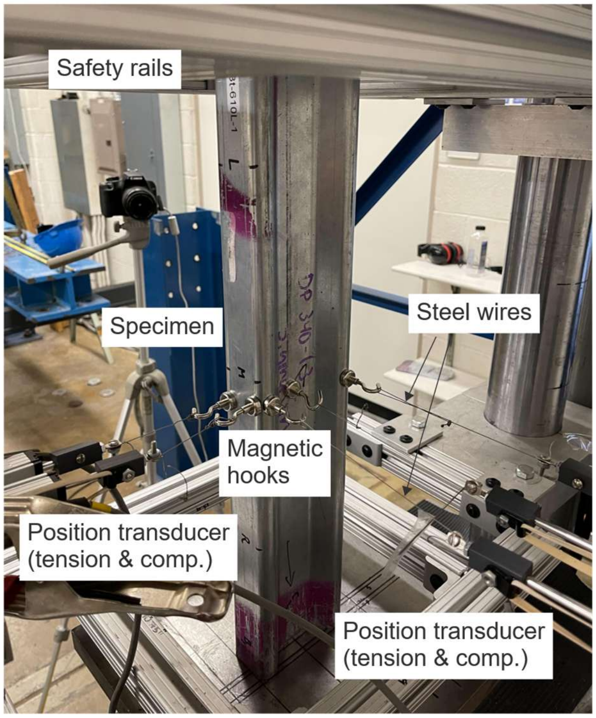

Fig. 2. Layout of position transducers

3.2 Test matrix

The testing program consists of 156 pure compression tests. A breakdown of the test matrix is shown in Table 1. Three parameters are controlled in the test matrix: material, cross-section, and member length. The selection of these parameters allows the study to investigate a variety of buckling behaviors. The material parameter allows the study to evaluate the influence of yield stress on the strengths of the compression members. There are 8 AHSS grades in this study, with nominal yield stress ranging from 340 MPa to 1200 MPa. The material properties of the AHSS grades are provided in Table 2. The properties of a subset of steel from the same batch of steel sheets (DP340-1.3, MS1030-1.0, MS1200-1.0 and MS1200-1.4) have been reported in a related study [22]. The material properties and test specimens are named per the nomenclature shown in Fig. 4. These specific grades were selected in consultation with industry, as having the potential to exist in the market at prices amenable to use in civil construction. The application of different cross sections is intended to induce different combinations of local and distortional buckling slenderness. The sigma sections were selected using a heuristic optimization process to maximize the material efficiency of AHSS. The 4 cross sections employed in this study are shown in Fig. 3, which shows the nominal dimensions. The member lengths are leveraged to potentially produce different buckling failure modes: short length (305 mm) for local buckling; intermediate length (610 mm) for distortional buckling; long length (1219 mm) for local or distortional buckling interacting with global buckling. A minimum of 2 repetitions are performed for the 305 mm and 610 mm long columns.

The column specimens were manufactured by press-braking steel sheets into lipped channel C and Sigma section members. The initial nominal member lengths were 1219 mm. The members were further cut into specimens at two additional lengths, 305 mm, and 610 mm. The ends of the specimens were machine-ground to ensure levelness. Additionally, the out-of-plumbness ratio of each specimen, defined as offset / length is also measured. The average out-of-plumbness ratio is L/347 in the minor axis bending direction and L/378 in the major axis direction. The cross-section dimensions and out-of-plumbness per specimen are recorded in the first author's dissertation [23].

Table 1. Test matrix

	C sections			Sigma sections			
	L = 305 mm	L = 610 mm	L = 1219 mm	L = 305 mm	L = 610 mm	L = 1219 mm	Subtotal
DP340-1.3t	4	5	3	4	6	2	24
DP550-1.2t	2	3	/	3	4	/	12
DP700*-1.4t	2	2	/	3	3	/	10
DP700-1.4t	4	6	2	4	6	2	24
MS1030-1.0t	4	5	2	5	4	3	23
MS1200-1.0t	2	3	2	6	5	2	20
MS1200-1.4t	4	6	2	4	6	2	24
MS1200-2.0t	4	5	2	/[a]	5	3	19
Subtotal	26	35	13	29	39	14	156

Notes:
1. "/" means not available
2. DP700-1.4t and DP700*-1.4t correspond to two separate sets of DP700 sheets.

Table 2. Material properties

Material	Steel type[a]	Gross thickness (mm)	Uncoated thickness (mm)	F_y[b] (MPa)	F_u (MPa)	ϵ_y[b] (%)	ϵ_u (%)
DP340-1.3	DP	1.3	1.29	365	575	0.38	14.52
DP550-1.2	DP	1.2	1.16	715	945	0.55	5.88
DP700*-1.4	DP	1.4	1.40	762	960	0.52	6.59
DP700-1.4	DP	1.4	1.38	813	1010	0.60	7.10
MS1030-1.0	MS	1.0	1.00	1246	1317	0.70	2.40
MS1200-1.0	MS	1.0	1.00	1342	1496	0.77	2.81
MS1200-1.4	MS	1.4	1.41	1467	1569	0.94	2.84
MS1200-2.0	MS	2.0	2.02	1538	1571	0.96	1.92

Note:

[a] DP refers to dual phase while MS refers to martensitic.

[b] yield stress is determined from 0.2% strain offset.

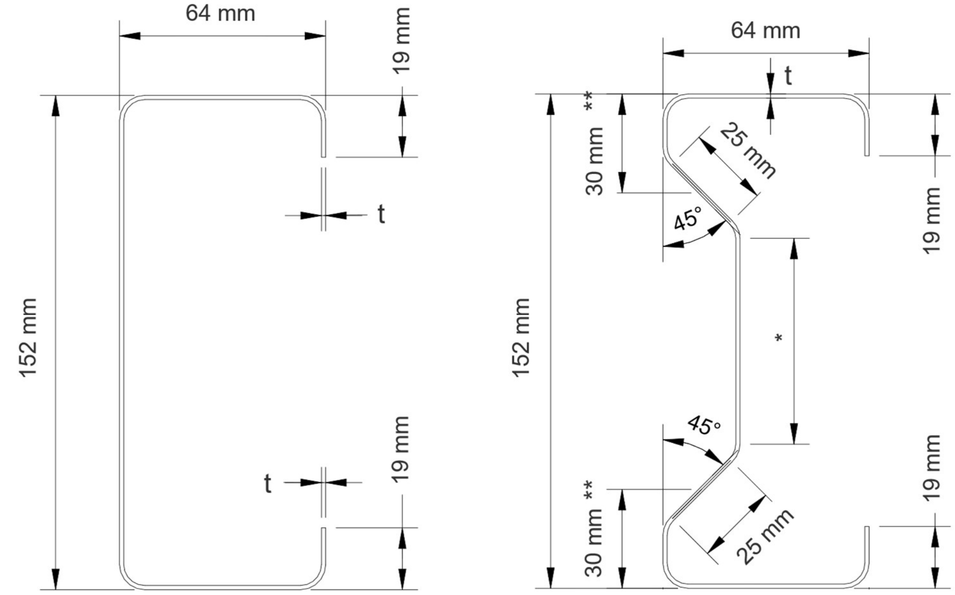

152 mm cee section
(152C)

152 mm sigma section
(152Sigma)

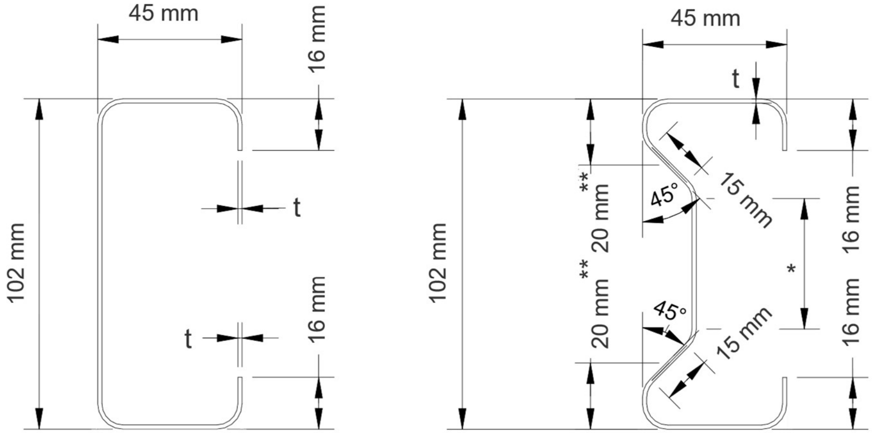

102 mm cee section
(102C)

102 mm sigma section
(102Sigma)

* Dimension varies depending on thickness
** Dimension from center of stiffener flat portion to flange outer surface

Fig. 3. Specimen cross sections and nominal dimensions (see Ding (2022) for per specimen measured dimensions)

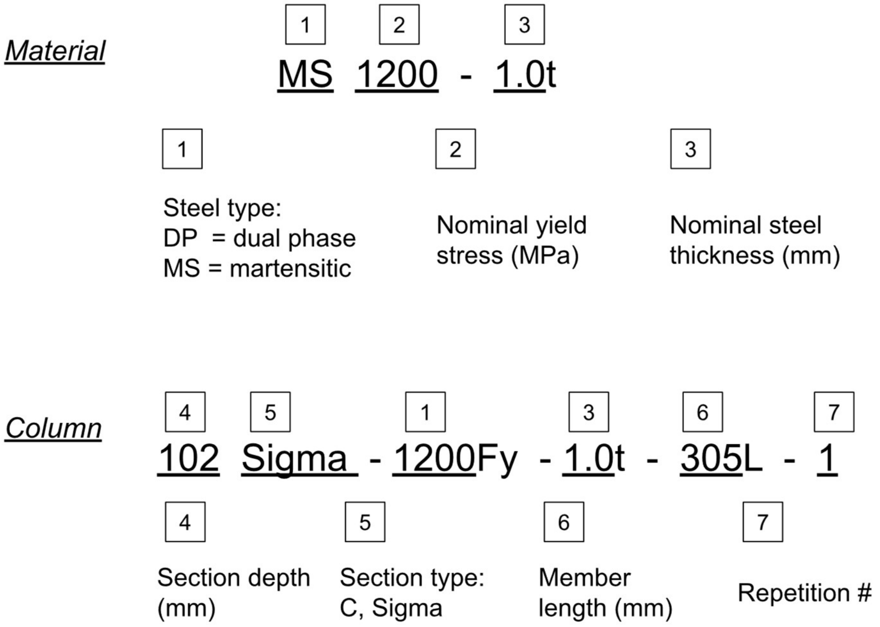

Fig. 4. Nomenclature of steel materials and column test specimens

4. Stability analysis of cross-sections

Finite strip analyses are performed on the four cross-sections used in this study using CUFSM [24]. The signature curves and corresponding critical buckling shapes (local and distortional) are provided in Fig. 5 - Fig. 8. For the C sections, the critical local buckling is controlled by the buckling at the webs. For the two Sigma sections, the dominant location varies: the shallower Sigma (102Sigma) has two critical local buckling modes with similar force magnitudes – one at the flanges and one at the web; the deeper Sigma (152Sigma) has only the critical local buckling mode which occurs at the web.

As for distortional buckling, the mode shapes of the four sections are typical distortional buckling modes of lipped channels – either opening-up (outward) or closing-in (inward) of the cross-sections. But there are two differences between the C and Sigma sections. Neither of the two Sigma sections have local minima on their signature curves corresponding to critical distortional buckling. The two-step method [25] is used to locate the critical distortional buckling modes. Compared to the C sections, the Sigma sections exhibit participation of a global mode, which manifests as minor-axis flexure.

Local and distortional buckling modes also cause warping. Distributions of the longitudinal displacement across the cross-sections are examined. For distortional buckling, the outward mode and inward mode have opposite warping displacement distributions. The outward mode causes compressive displacement at the lips, while the inward mode causes tensile displacement at the lips. For a boundary condition with asymmetric warping restraints (e.g., compressive only as in the bearing on end platens used herein), it is hypothesized that the inward mode may have lower critical buckling force, because warping can cause the lips to lift off which renders it less effective against flange bending.

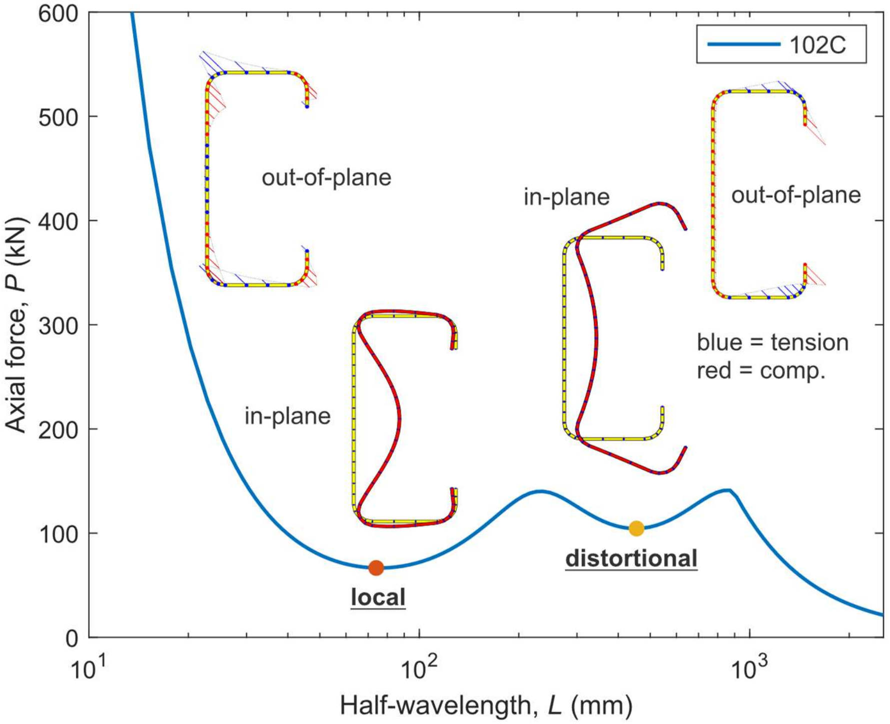

Fig. 5. Signature curve and buckling shapes of 102C

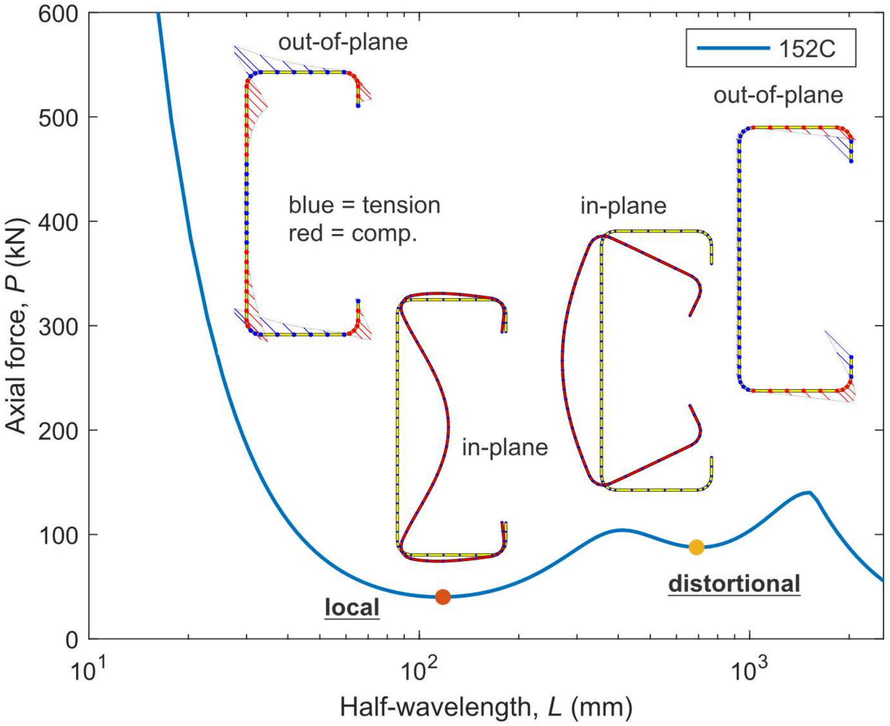

Fig. 6. Signature curve and buckling shapes of 152C

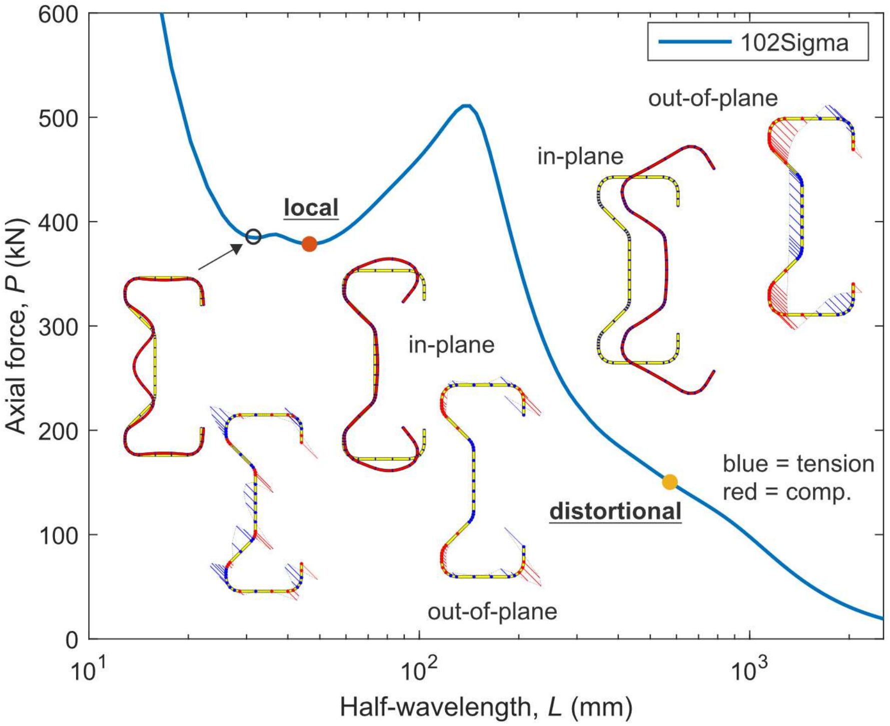

Fig. 7. Signature curve and buckling shapes of 102Sigma

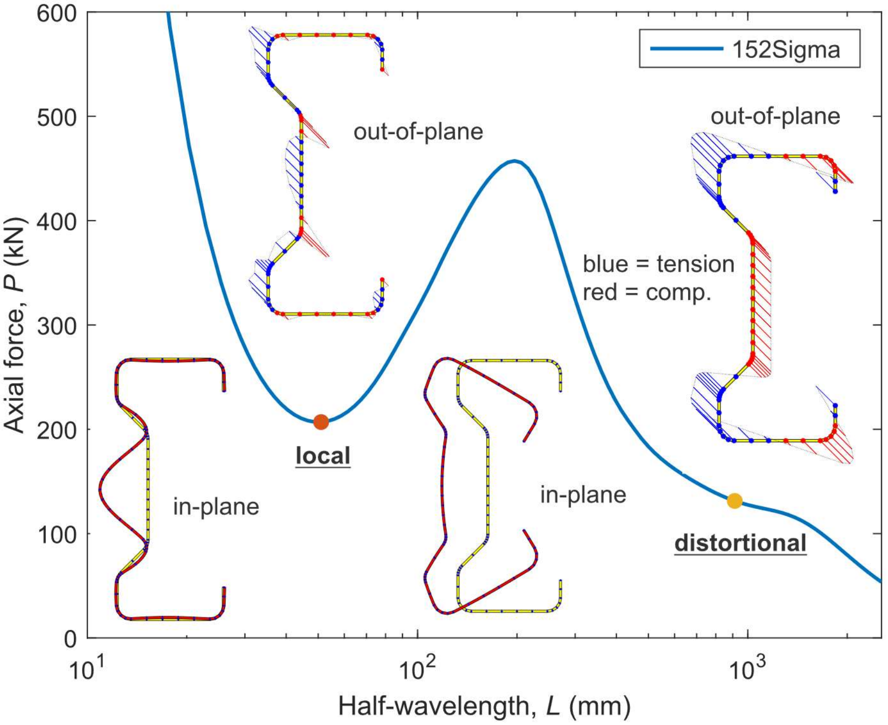

Fig. 8. Signature curve and buckling shapes of 152Sigma

5. Test results

5.1 Load-deformation curves

Based on length, the column specimens are divided into three categories: short columns (L = 305 mm), intermediate columns (L = 610 mm), and long columns (L = 1219 mm). The load-deformations of the three categories are respectively shown in Fig. 9, Fig. 10 and Fig. 11. The ultimate load of each test is tabulated in the Appendix.

Comparison is made between the load-deformation curves of different specimen groups. With other parameters the same or close, higher yield stress leads to higher ultimate loads at all three member lengths. This is exemplified by the comparison between the curves of MS1200-1.4 (1200 MPa nominal F_y), DP700-1.4 (700 MPa nominal F_y), and DP340-1.3 (340 MPa nominal F_y). For 152C columns at 610 mm lengths, the peak loads of the MS1200-1.4 column are approximately 35% higher than these of the DP700-1.4 columns and 190% higher than these of the DP340-1.3. The fact that column strengths can be significantly increased by higher yield stresses alone (without further section optimization) shows the obvious potential for AHSS adoption in CFS framing.

The comparison also finds that higher yield stress coincides with steeper post-peak response. For example, as seen in Fig. 11, the load-deformation curves of the MS1200 specimens experience sharp post-peak strength loss, while the curves of the DP340-1.3 specimens have relatively gentle strength loss in the post-peak regime. The cross-section type is also observed to be a factor. The specimens with the Sigma sections are found to generally have steeper post-peak response than the specimens with regular C sections.

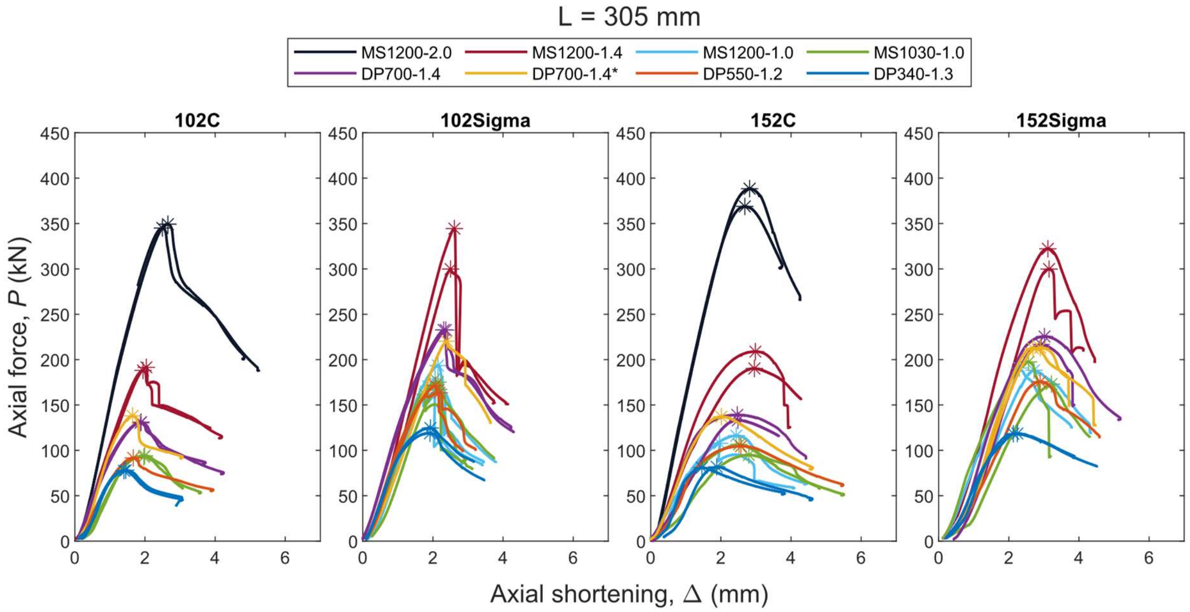

Fig. 9. Load deformation curves of short column (L = 305 mm) tests

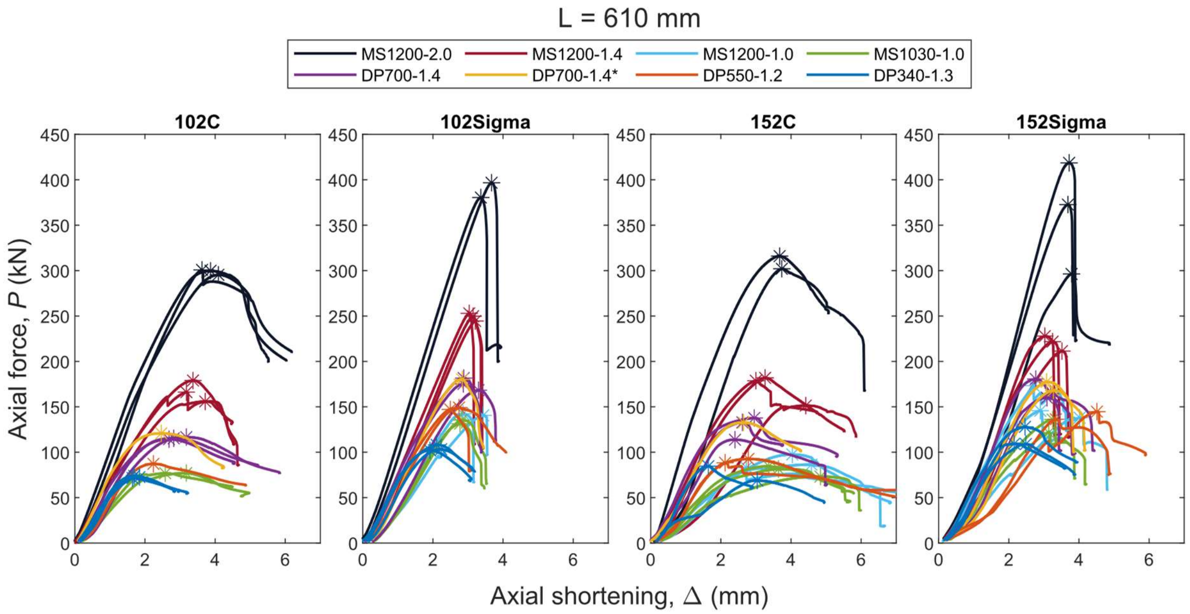

Fig. 10.Load deformation curves of intermediate columns (L = 610 mm) tests

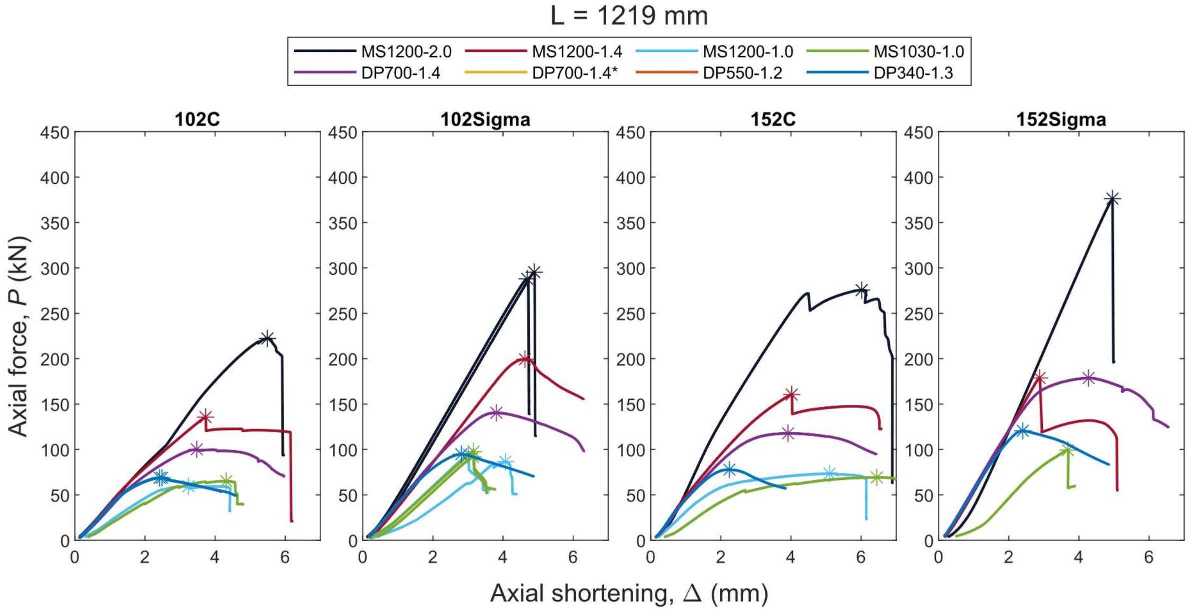

Fig. 11. Load-deformation curves of long column (L = 1219 mm) tests

5.2 Observed failure modes

5.2.1 Short columns (310 mm)

For the short column tests, the dominant failure mechanisms are associated with local buckling. In the test images of Fig. 12, two rows of test deformations are shown: deformation at peak loads P_{max}, and deformations at post-peak with loads equal to $0.8P_{max}$. For both C specimens and Sigma specimens, the failures are initiated by plastic mechanisms developed from web local buckling, but lead to failure mechanisms that engage the flange and lips. Compared to C sections, Sigma sections exhibit more buckling half-waves, which is consistent with their shorter plate widths. Higher yield stresses are found to coincide with larger buckling deformations at the specimens' peak loads. For example, the 1200 MPa (far right) specimens consistently display more developed web buckling waves than the 340 MPa (far left) specimens, where the starkest difference can be seen in Fig. 12 (c).

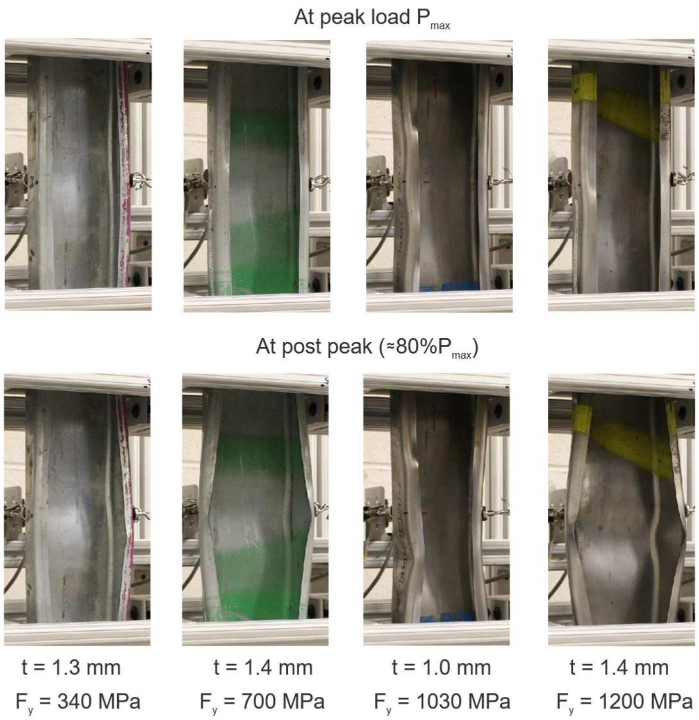

(a) 102C

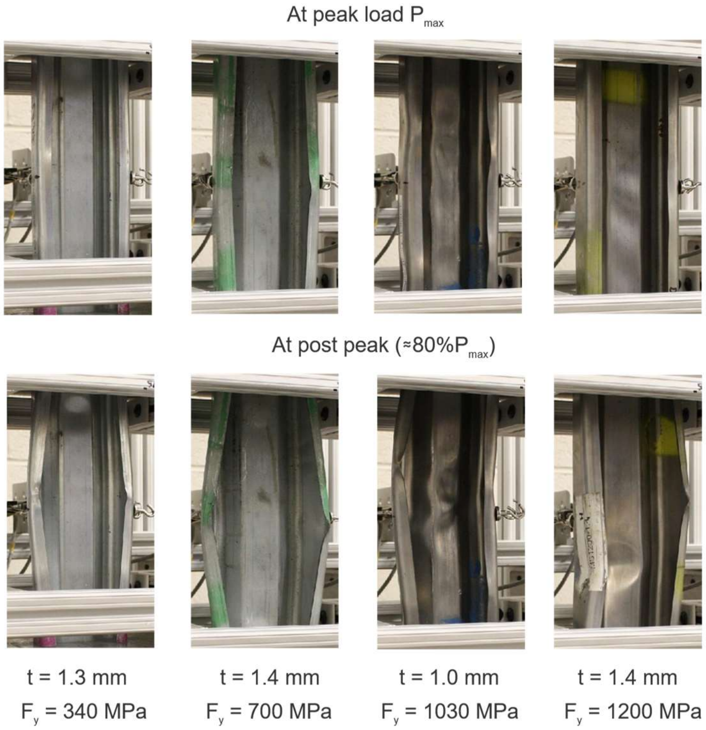

(b) 102Sigma

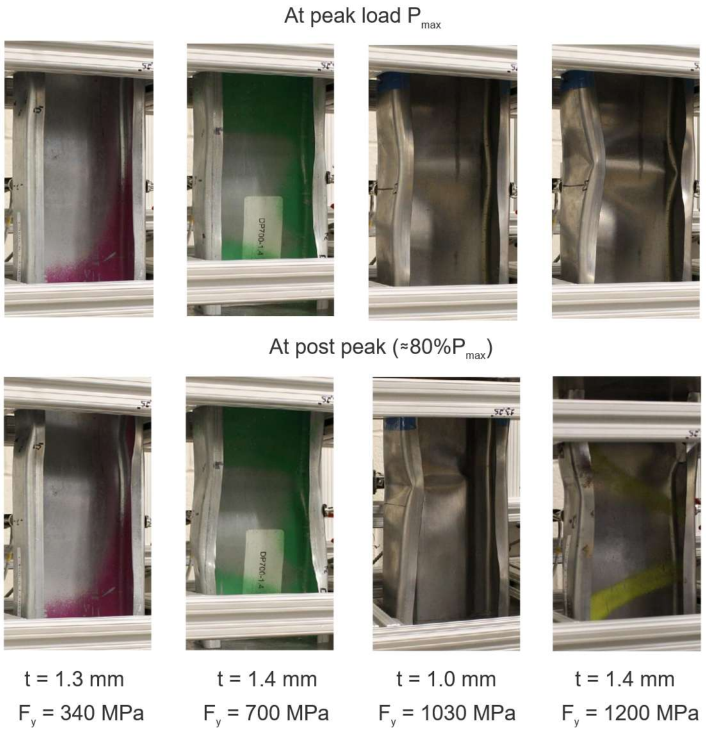

(c) 152C

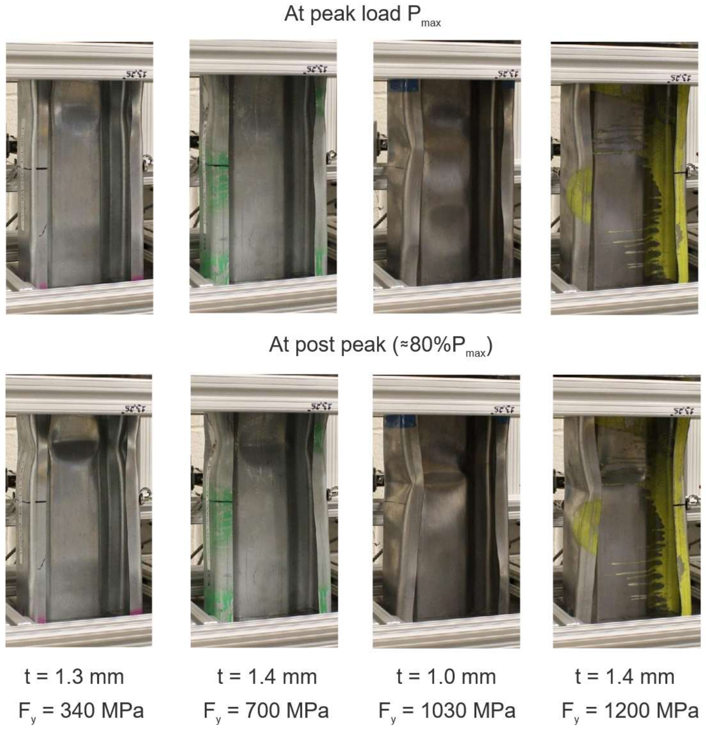

(d) 152Sigma

Fig. 12. Failure modes of short columns (310 mm): (a) 102C sections (b) 102Sigma sections (c) 152C sections (d) 152Sigma sections

5.2.2 Intermediate columns (610 mm)

For intermediate column tests, distortional buckling is observed as the dominant buckling mode leading to plastic mechanisms. Strong visual evidence of distortional buckling deformations can be found in the deformations of all four sections (see Fig. 13 (a) – (d)), which are represented by a single large buckling half-wave on the flanges.

In addition to distortional buckling, the high yield stress columns also develop web and flange local buckling. The 1030 MPa and 1200 MPa Sigma specimens (see Fig. 13 (b) and (c)) exhibit web local buckling at the peak loads, which are represented by the shorter half-waves on the webs. For the same group of steels, the corresponding C columns (Fig. 13 (c)) develop shorter flange local buckling half-waves on top of the distortional buckling half wave at the peak loads. The co-existence of local buckling and distortional half-waves is visual evidence of potential local-distortional buckling interactions. In the post-peak responses ($0.8P_{max}$), the single larger distortional buckling half-wave further solidifies until the multiple shorter local buckling half-waves merge with the distortional one. For the Sigma columns, the transition is more significant. In Fig. 13 (b) and (d), the web stiffeners of the 1030 MPa and 1200 MPa specimens flatten at the mechanism locations to the extent of resembling C sections.

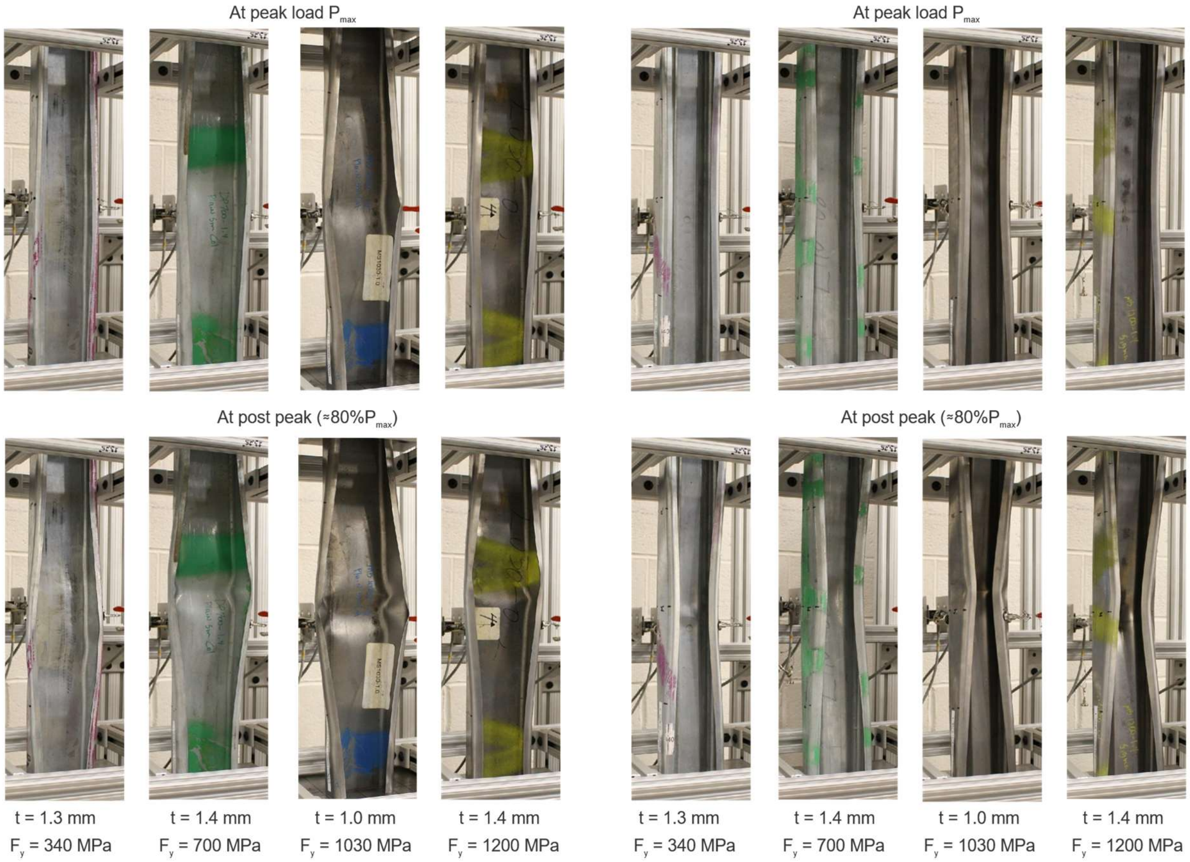

(a) 102C (b) 102Sigma

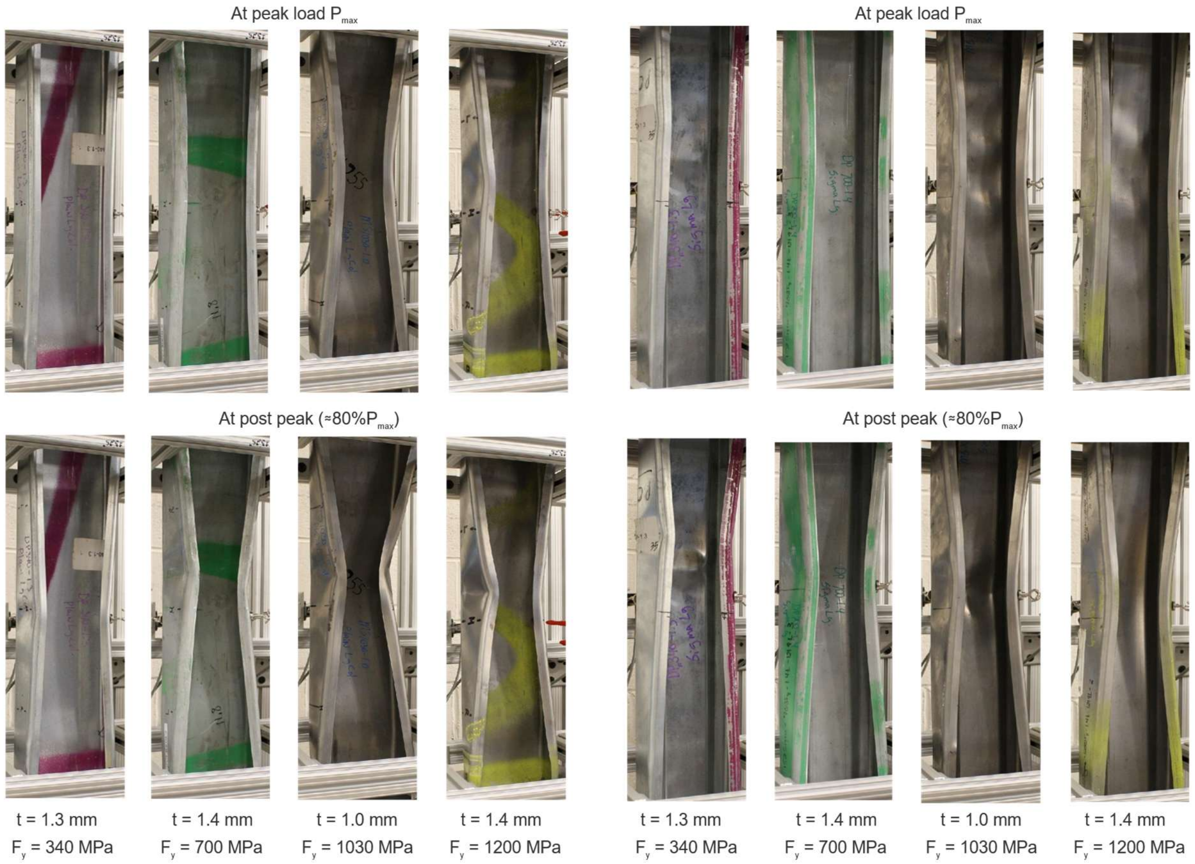

(c) 152C (d) 152Sigma

Fig. 13. Failure modes of intermediate (610 mm) columns: (a) 102C sections (b) 102Sigma sections (c) 152C sections (d) 152Sigma sections

5.2.3 Long columns (1219 mm)

Both distortional buckling, and local-global buckling interaction are observed among the 1219 mm long specimens. The failures of the C section specimens (102C and 152C) are largely characterized by local-global buckling interaction Fig. 14 (a) and Fig. 14 (c), except for the 1030 MPa specimens whose responses are dominated by the large distortional buckling half-waves. For Sigma sections, distortional buckling is found to be the dominant mode in the failures as seen in Fig. 14 (b) and Fig. 14 (d). Similar to the intermediate columns, the distortional buckling is also followed by minor axis flexure, which indicates participation of global buckling at least in the post-peak response.

There are two types of distortional buckling deformation, inward (section closing in) or outward (section opening up). It is found that the majority of 1219 mm long Sigma specimens with $F_y >$ 1000 MPa fail with inward distortional buckling. The remaining 1219 mm long Sigma specimens, which have lower F_y, are found to fail with outward distortional buckling. Between the inward and outward distortional buckling, there are clear differences in the load-deformation curves. The inward distortional buckling fails with a dramatic loss of strength in the post-peak response (e.g., 152Sigma with MS1030-1.0 in Fig. 14 (d)) while the outward distortional buckling comes with a more gradual post-peak response (e.g., 152Sigam with DP700-1.4 in Fig. 14 (d)). It is hypothesized that the direction of distortional buckling influences the effectiveness of the boundary conditions (in particular whether warping deformations at the lip edge in bearing with the end platens are in tension or compression as the section distorts) and the participation of global buckling.

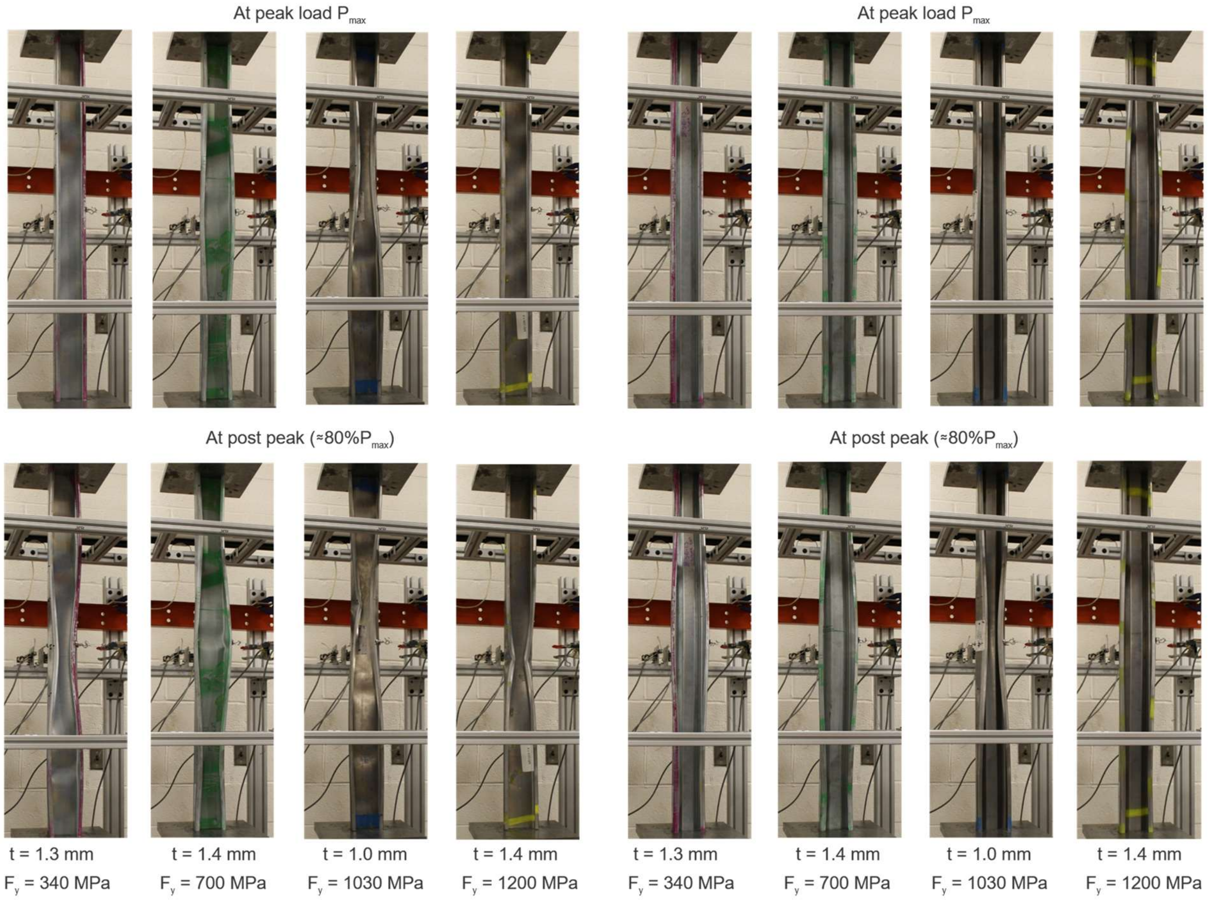

(a) 102C (b) 102Sigma

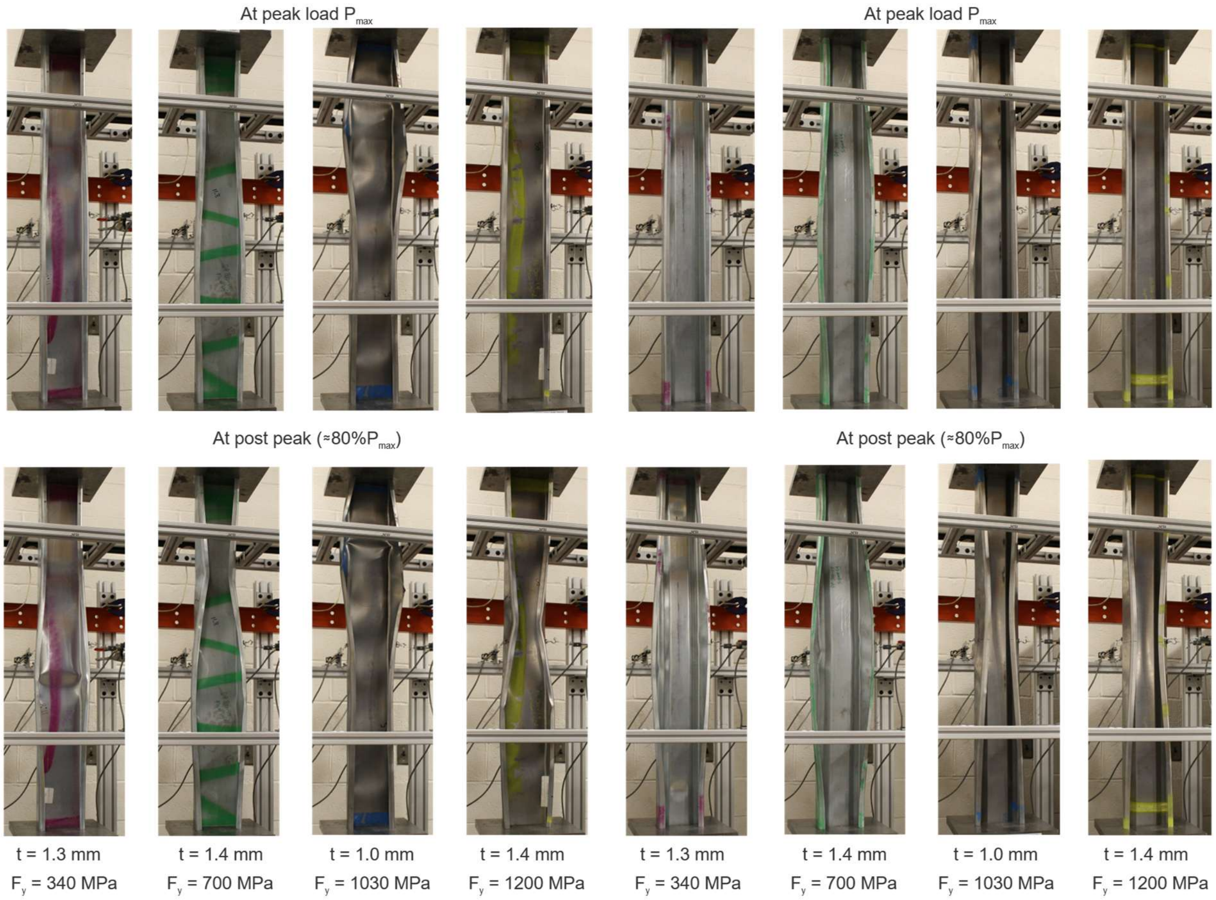

(c) 152C (d) 152Sigma

Fig. 14. Failure modes of long columns (1219 mm): (a) 102C sections (b) 102Sigma sections (c) 152C sections (d) 152Sigma sections

6. Boundary conditions for bare-end bearing

This experiment program adopts bare end bearing as the boundary condition (BC) for column specimens. Such boundary condition may be different from the idealistic SS or CC conditions commonly assumed in member buckling strength predictions. For short columns where local buckling controls, there is experimental evidence [21] that bare end bearing and CC are equivalent. For longer columns where distortional or global buckling may control, the relation between bare end bearing and CC is less certain.

As analytical equations and numerical tools are centered around idealized BC assumptions for calculating the elastic critical buckling loads. The choice of such assumptions has large implications for Direct Strength Method (DSM) which uses the loads to locate the members in the slenderness space. To determine appropriate boundary conditions for calculating critical elastic buckling loads, a numerical study is performed using finite element analysis.

6.1 Numerical study of boundary conditions

The numerical study consists of two parts: (1) developing a FE model which uses contact to simulate the bare end bearing condition to establish good match with tests (2) changing the boundary conditions of the validated FE model to idealized boundary conditions (SS and CC) to determine the appropriate boundary conditions for the bare end bearing condition.

The contact model is developed in ABAQUS (see Fig. 15). The column specimen is modeled using quadratic shell elements (S8R). The top and bottom loading platens are modeled using analytical rigid surfaces. Node-to-surface contact pairs are defined between the end sections of the column and the loading platens. The contact pair is defined with a coefficient of friction equal to 0.3, which is a typical value for steel-to-steel contact. The contact definition allows for separation and sliding, which simulates the bare end bearing condition. The mid-section of the column is restrained for longitudinal translation. Each of the loading platens is rigid-body constrained to a reference node located at the centroid of the column end section. The top and bottom reference nodes are constrained for all translations and rotations except for the imposed longitudinal translations. The shell element model is created with Type 1 and Type 2 imperfections [26]. The imperfection distributions are generated from finite strip analysis using CUFSM and applied as perturbations of node coordinates at magnitudes based on measurements and 50% CDF minimum. The analysis is performed using general static analysis with artificial damping ratio (0.01) which the author finds easier to converge models than RIKS for contact models. Sensitivity analyses are performed for friction coefficient and artificial damping ratios which find these parameters having no meaningful effect on the FE results (see Appendix 1).

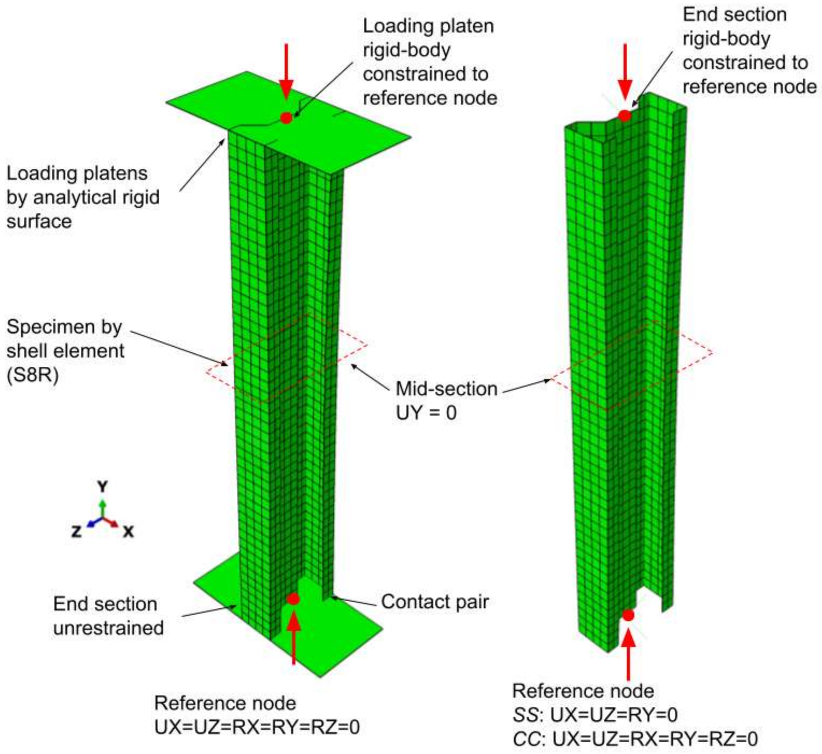

Fig. 15. FE models of contact models and SS/CC models

For the idealized boundary conditions, the same FE model is used but the contact interactions are replaced with appropriate constraints to simulate SS and CC conditions. For both SS and CC conditions, the end sections of the column are rigid-body constrained to the reference nodes. The SS models are restrained against lateral translations and torsion. The CC models are additionally restrained against flexures.

The numerical program is applied for a subset of the tested specimens, including two yield stress levels (F_y = 340 MPa and 1200 MPa) at two lengths (L = 610 mm and 1229 mm) and all four cross-sections, which makes a reasonable representation of the key parameters of the testing program.

6.2 *Numerical study results*

The results of the FE contact models are compared with the test results to validate the modeling approach. The comparison of peak loads shows good agreement between the FE models and the tests, with the mean ratio of FE to test peak loads being 1.07 and COV being 0.16. The comparison of load-deformation curves also shows reasonable agreement (see Fig. 16), and the deformations at the peak loads match well with the test results (see Fig. 17 and Fig. 18). Variations do exist on a per-specimen level. However, the overall match between the models and tests indicates that the FE model with contact can effectively simulate the bare end bearing condition and predict the peak loads with good accuracy.

The CC and SS models are compared to the contact models to determine the appropriate boundary condition assumptions. The ratios of FE SS and CC peak loads to the FE contact peak loads are calculated for each specimen. The results show that the FE CC peak loads are within 5% higher than FE contact peak loads on average (mean = 1.03) with a COV of 0.05, while the FE SS peak loads are on average 17% lower than the FE contact peak loads (mean = 0.83) with a COV of 0.18. Comparison of load-deformation curves suggests that SS models may fail at buckling modes different from those of contact and CC models (see Fig. 16).

Investigation of the deformed shapes at the peak loads more clearly captures the differences in failure modes. Fig. 17 shows excellent match of distortional buckling failure between the CC/Contact models and the tests. However, in this case, the SS model fails in flexural buckling. The contact and CC models exhibit buckling modes while the SS model exhibits a different failure mode. The deformation of the end sections further highlights the differences. The contact model displays clear signs of warping as evidenced by the lip lift-off and CC model shows uniform displacement, while the SS model deforms in a distribution representing minor-axis flexure. For other models, the differences are more subtle. In Fig. 18, all three FE models fail in distortional buckling though the SS model has clear participation of flexural buckling indicated by the end section deformation.

The results indicate that the CC is an appropriate assumption for calculating critical elastic buckling loads for the bare end bearing condition in this testing program, while the SS boundary condition is not appropriate as it significantly underestimates the peak loads.

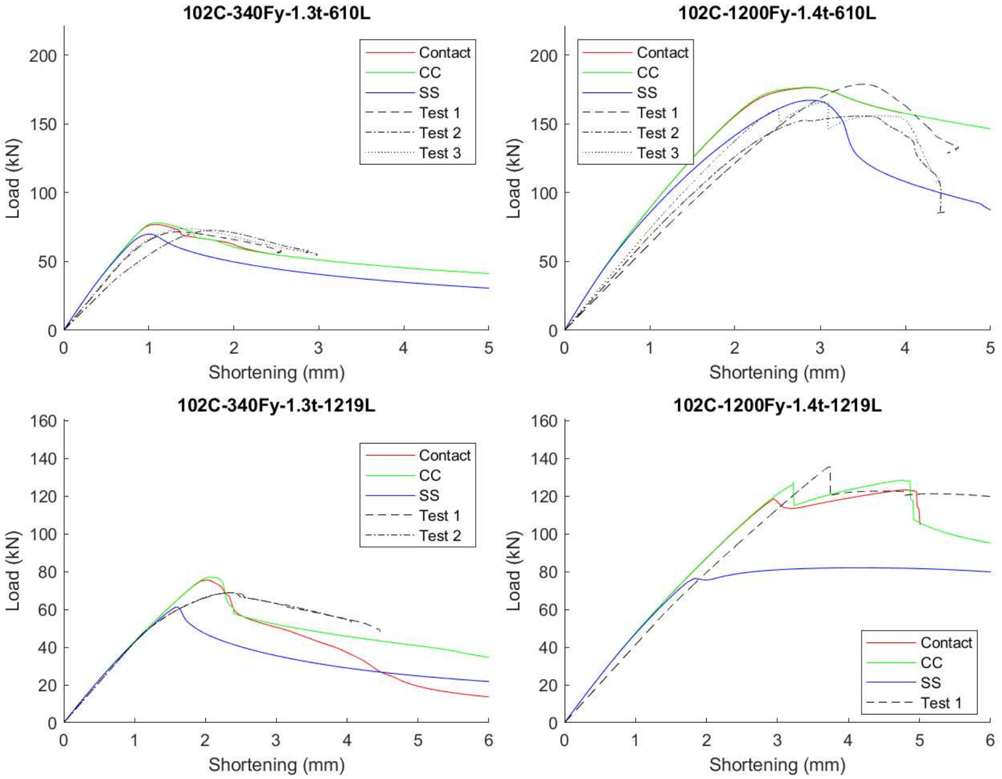

(a)

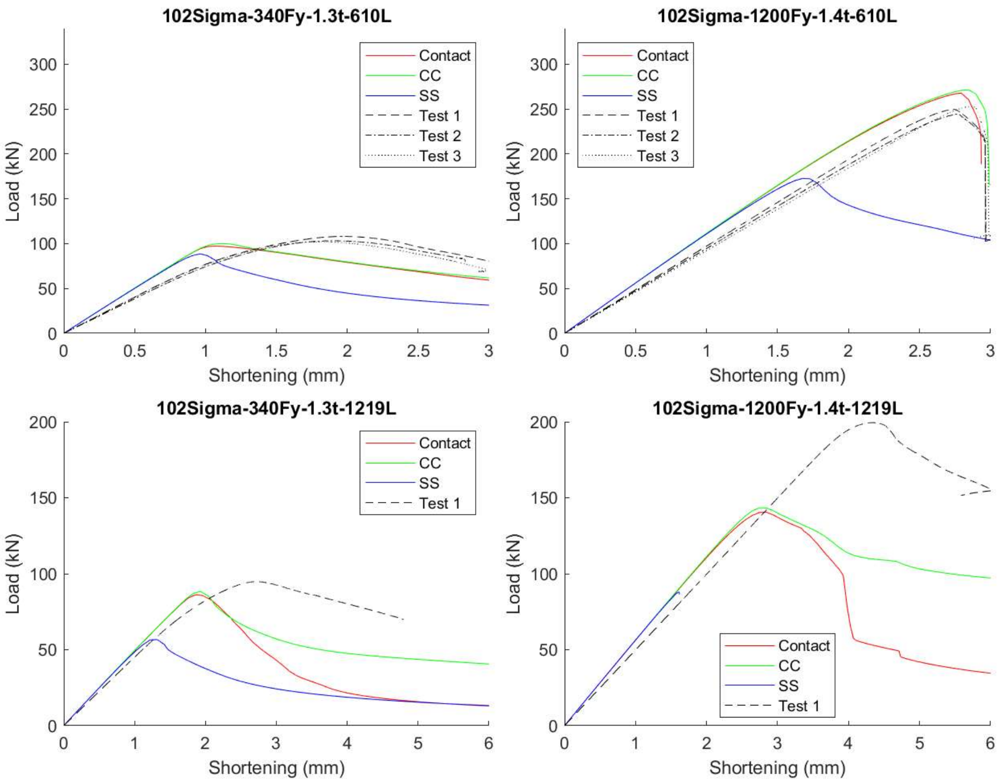
102Sigma-340Fy-1.3t-610L
102Sigma-1200Fy-1.4t-610L
102Sigma-340Fy-1.3t-1219L
102Sigma-1200Fy-1.4t-1219L
Load (kN)
Shortening (mm)
Contact
CC
SS
Test 1
Test 2
Test 3
0
50
100
150
200
250
300
0.5
1
1.5
2
2.5
3
4
5
6

(b)

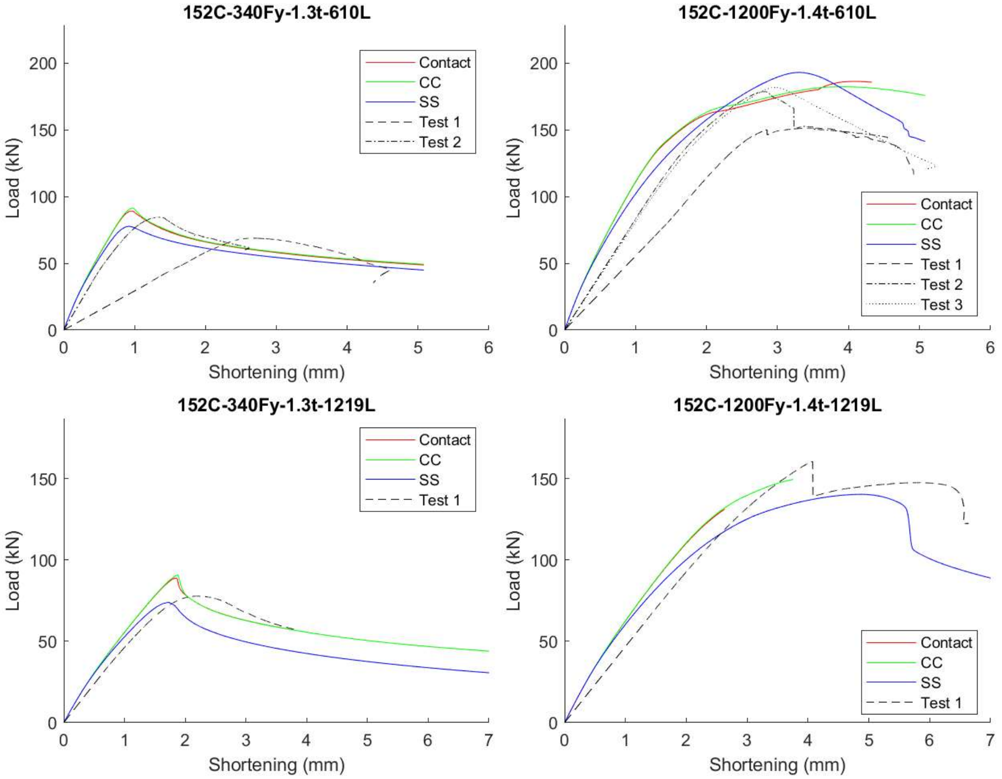
152C-340Fy-1.3t-610L
152C-1200Fy-1.4t-610L
152C-340Fy-1.3t-1219L
152C-1200Fy-1.4t-1219L
Load (kN)
Shortening (mm)
Contact
CC
SS
Test 1
Test 2
Test 3
0
50
100
150
200
1
2
3
4
5
6
7

(c)

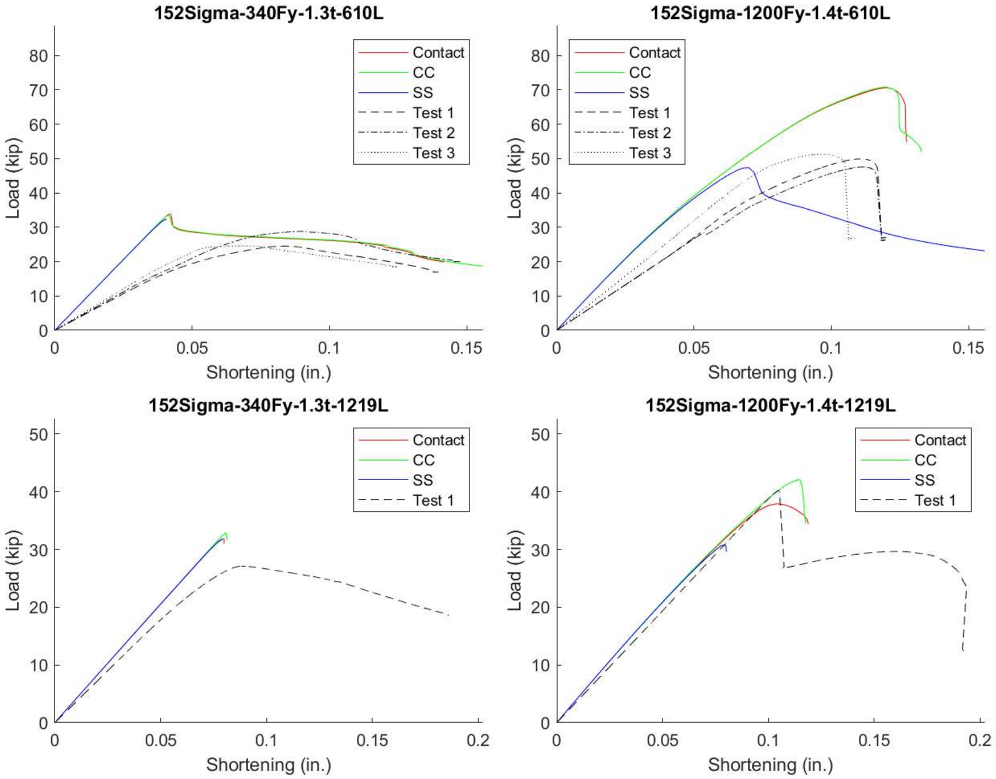

(d)

Notes: For test curves, pre-peak segments before 40% peak load are represented by tangent stiffnesses approximated at 40% peak load for ease of comparison.

Fig. 16. Load deformation curves of FE models compared to test results: (a) Section 102C (b) Section 102Sigma (c) Section 152 Sigma (d) Section 152C

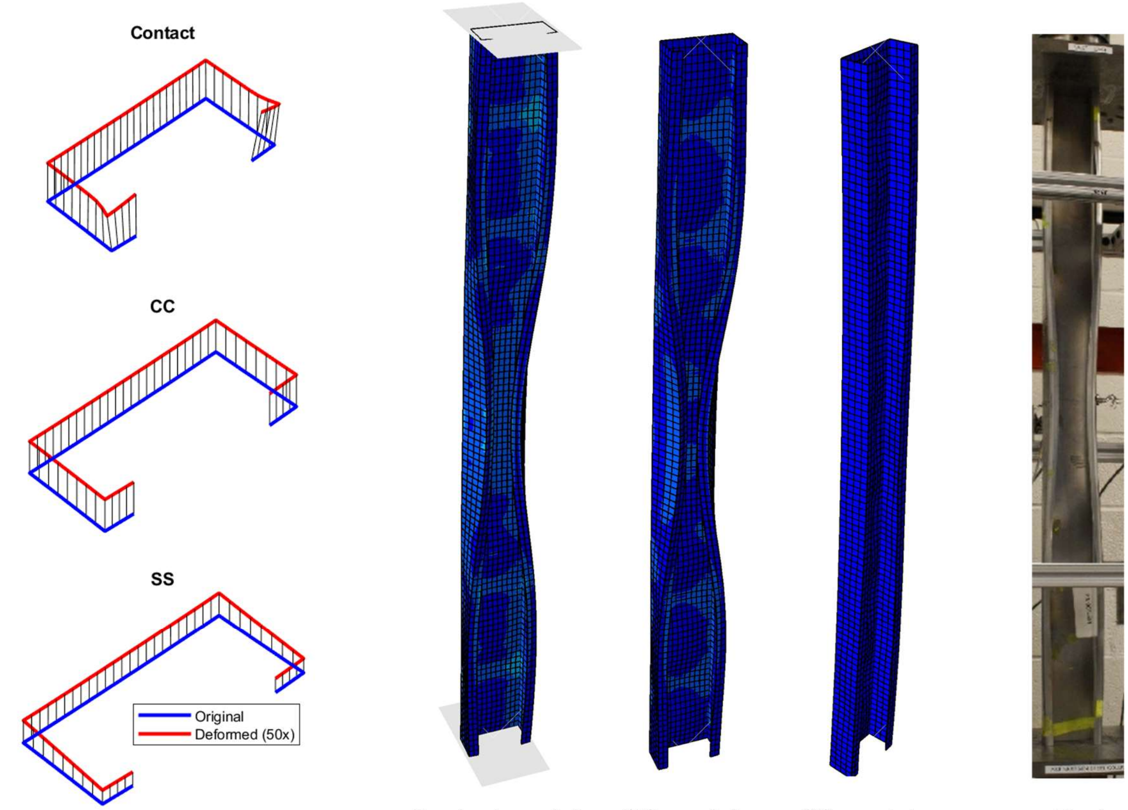

Contact model CC model SS model Test

* Deformation of bottom end section at peak load

* Deformation shown at peak loads
* For test 102C-1200Fy-1.4t-1219L

Fig. 17. Deformation of a C section model at peak load

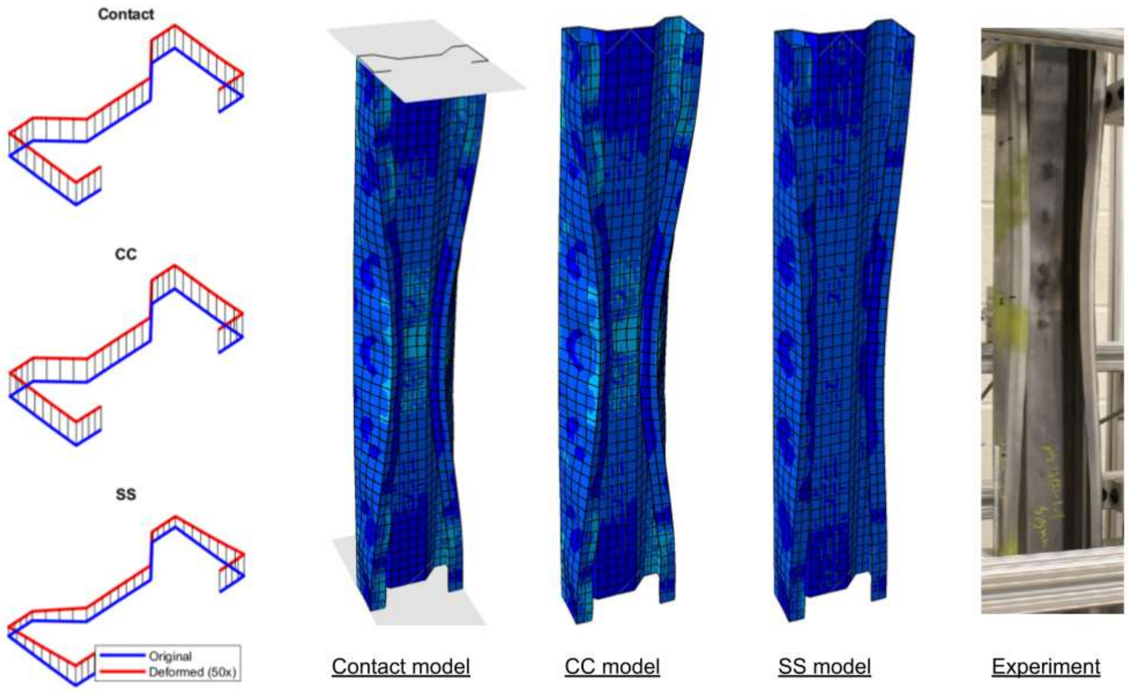

Contact model CC model SS model Experiment

* Deformation of bottom end section at peak load

* Deformation shown at peak loads
* For test 102Sigma-1200Fy-1.4t-610L

Fig. 18. Deformation of a Sigma section model at peak load

7. Comparison to design predictions

7.1 DSM strength predictions

Strength predictions are performed for the AHSS column tests using Direct Strength Method (DSM) in AISI S100 (2022) [2] and AS/NZS 4600 [3]. The DSM implementations in AISI S100 (2022) [2] and AS/NZS 4600 [3] are the same except for the choices of variable symbols. In this study, the AISI DSM format is used. The column tests are treated as pure compression members and their compressive strengths are determined as the minimum of the three buckling limit state strengths as expressed in Eq. (2): global buckling (Eq. (3)), local-global buckling (Eq. (4)), and distortional buckling (Eq. (5)).

$$P_n = \min(P_{ne}, P_{n\ell g}, P_{nd}) \qquad \text{Eq. (2)}$$

where P_n is nominal compressive strength, P_{ne} is nominal global buckling load $P_{n\ell g}$ is nominal local-global buckling load, and P_{nd} is the nominal distortional buckling load.

$$P_{ne} = \begin{cases} 0.658^{\lambda_c^2} P_y & \lambda_c \leq 1.5 \\ \left(\frac{0.877}{\lambda_c^2}\right) P_y & \lambda_c > 1.5 \end{cases} \qquad \text{Eq. (3)}$$

where $\lambda_c = \sqrt{P_y/P_{cre}}$, P_y is yield load, P_{cre} is elastic critical global buckling load

$$P_{n\ell g} = \begin{cases} P_{ne} & \lambda_{\ell g} \leq 0.776 \\ (1 - 0.15\lambda_{\ell g}^{-0.8})\lambda_{\ell g}^{-0.8} P_{ne} & \lambda_{\ell g} > 0.776 \end{cases} \qquad \text{Eq. (4)}$$

where $\lambda_{\ell g} = \sqrt{P_{ne}/P_{cr\ell}}$, $P_{cr\ell}$ is elastic critical local buckling load

$$P_{nd} = \begin{cases} P_y & \lambda_d \leq 0.561 \\ (1 - 0.25\lambda_d^{-1.2})\lambda_d^{-1.2} P_y & \lambda_d > 0.561 \end{cases} \qquad \text{Eq. (5)}$$

where $\lambda_d = \sqrt{P_y/P_{crd}}$, P_{crd} is elastic critical distortional buckling load

7.2 Elastic critical buckling loads

DSM requires input of elastic critical buckling loads. The set of buckling loads include local buckling load ($P_{cr\ell}$), distortional buckling load (P_{crd}) and global buckling load (P_{cre}). In this study, all three buckling loads are calculated numerically through finite strip analyses performed in CUFSM [24]. The critical local buckling load is calculated from signature curves produced by conventional finite strip analyses since the boundary conditions usually have a negligible impact on it.

For distortional and global buckling, general boundary condition finite strip analysis developed by [27,28] is used, because member lengths and boundary condition, particularly warping conditions, typically have great effects on distortional and global buckling. Based on the numerical study, C-C boundary condition is assumed.

To select the critical distortional and global buckling modes, finite strip modal identification method [29] is performed to calculate the participations for all buckling modes considered. The critical mode is selected as the one with the lowest critical load among those with not less than 50% participation of the target mode. For example, to select the critical distortional buckling modes, the analysis output is first filtered to include only the buckling modes with no less 50% distortional participation. Then along the remaining buckling modes, the one with the lowest critical load is selected as the critical elastic distortional buckling mode. The elastic critical bucking loads are tabulated in Table 4 of the Appendix 2.

7.3 Comparison to test results

DSM strength predictions are created and compared to test results. The comparison is shown in Fig. 19, where the test data are plotted against the DSM local and distortional buckling curves. All C column tests are predicted to fail in local-global buckling failures, while predicted failures of the Sigma column tests are split between local-global and distortional buckling. The DSM curves match well with the results of the C column tests but are unconservative for the Sigma column tests.

The current DSM strength predictions are unconservative. Mean test-to-predicted ratios are summarized in Table 3. The overall mean test-to-predicted ratio P_u/P_n is 0.89 and the corresponding COV is 0.16 (see Table 3 (a)). At high yield stresses, the current DSM overpredicts column strengths. For example, the mean test-to-predicted ratio of the columns with F_y = 1538 MPa is only 0.82. The DSM predictions are also worse for longer members. As member length increases from 305 mm to 1219 mm, the mean test-to-predicted ratio drops from 0.97 to 0.82. Between C and Sigma column tests, there is a dichotomy in DSM performance. For C section tests, the mean test-to-predicted ratio is 0.97; but for Sigma section tests, the mean is 0.81. Overall, the current DSM predictions need to be revised to improve accuracy. The groups of tests that particularly need improvement in DSM performance are those with higher yield stresses, longer member lengths and Sigma sections.

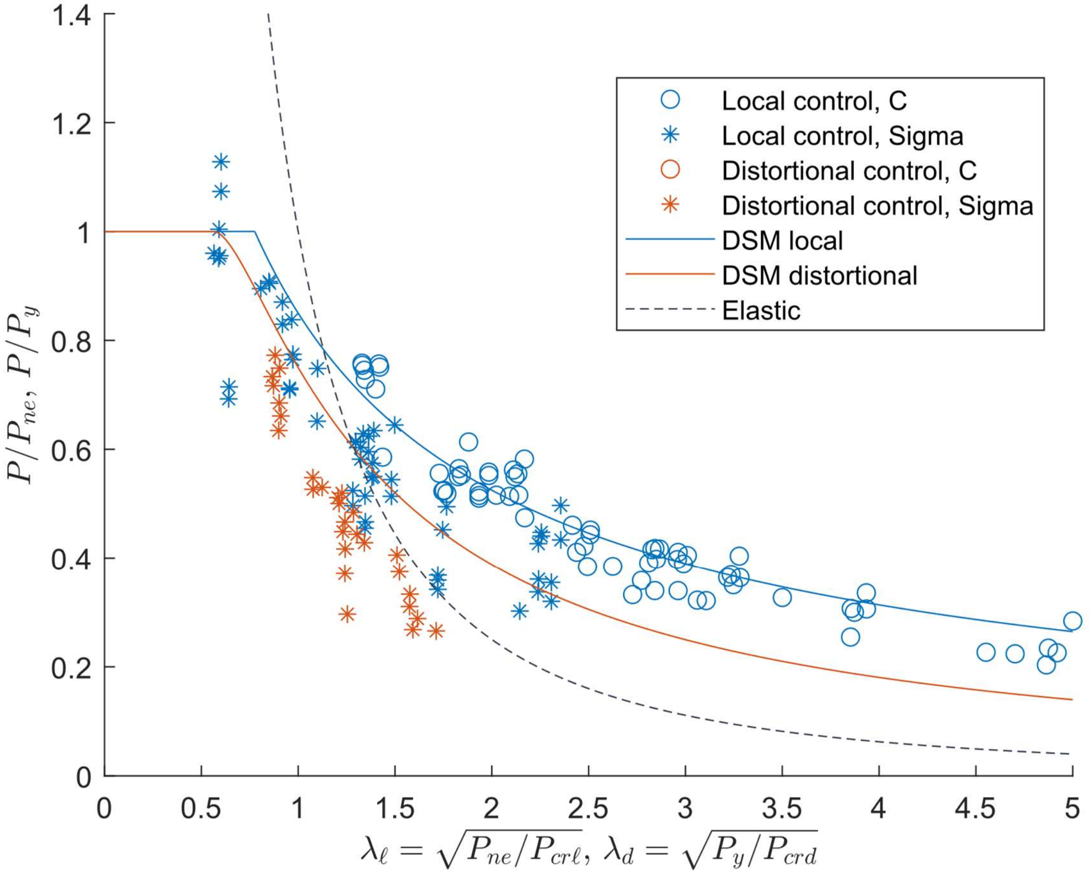

Fig. 19. DSM strength predictions compared to test results

Table 3. Summary of mean test-to-predicted ratios under various DSM design approaches

(a) Classical DSM

Material	F_y (MPa)	All sections	C only	Sigma only
DP340-1.3	365.00	1.02	1.09	0.95
DP550-1.2	715.00	0.95	1.02	0.90
DP700-1.4*	762.00	0.91	1.05	0.82
DP700-1.4	813.00	0.90	0.99	0.82
MS1030-1.0	1246.00	0.84	0.90	0.78
MS1200-1.0	1342.00	0.83	0.91	0.78
MS1200-1.4	1467.00	0.85	0.96	0.75
MS1200-2.0	1538.00	0.82	0.92	0.68
All materials	/	(0.89, 0.16)	(0.97, 0.10)	(0.81, 0.16)

(b) Method 1: DSM + AISI F_y reduction

Material	F_y (MPa)	All	C only	Sigma only
DP340-1.3	365.00	1.02	1.09	0.95
DP550-1.2	715.00	1.02	1.09	0.97
DP700-1.4*	762.00	0.97	1.11	0.88
DP700-1.4	813.00	0.96	1.05	0.87
MS1030-1.0	1246.00	0.99	1.05	0.93
MS1200-1.0	1342.00	0.98	1.07	0.93
MS1200-1.4	1467.00	1.01	1.12	0.89
MS1200-2.0	1538.00	0.96	1.08	0.79
All materials	/	(0.99, 0.15)	(1.08, 0.08)	(0.90, 0.15)

(c) Method 2: DSM + L-D interaction + reduced F_y

Material	F_y (MPa)	All	C only	Sigma only
DP340-1.3	365.00	1.04	1.12	0.96
DP550-1.2	715.00	1.05	1.15	0.98
DP700-1.4*	762.00	1.02	1.18	0.91
DP700-1.4	813.00	1.03	1.16	0.91
MS1030-1.0	1246.00	1.12	1.24	1.01
MS1200-1.0	1342.00	1.10	1.27	1.01
MS1200-1.4	1467.00	1.13	1.30	0.96
MS1200-2.0	1538.00	1.06	1.23	0.84
All materials	/	(1.07, 0.16)	(1.21, 0.09)	(0.95, 0.11)

Note:

1. “/” = data not available.

2. For each sub-table, the last row corresponding to “All materials” display both mean and COV values in the format (mean, COV).

8. Alternative DSM strength predictions

To obtain more accurate strength predictions under DSM, three potential options are explored. The three options are (1) using reduced yield stress (2) assuming S-S boundary conditions (3) considering additional buckling interactions. The statistical analysis results are summarized in Table 3. To better understand the change, in addition to results for all data, Table 3 summarizes statistical results under various groups of tests with different sections and member lengths. The nominal strengths are listed for each test in the Appendix 2.

8.1 Method 1: Reduced yield stress

The AISI S100 (2022) [2] Specification mandates reduced yield stress for steels not meeting ductility thresholds. For steels with elongation from 3% to less than 10%, it is required that $0.9F_y$ should be for member strength predictions; for steels with elongation below 3%, the lower value of $0.75F_y$ and 414 MPa is required for member strength predictions, and applications are only allowed for multi-web configurations (e.g., roofing).

The performance of DSM under reduced yield stress is explored. In this study, 0.9 yield stress reduction are applied to the high yield-stress DP steels, including DP550-1.2, DP700-1.4* and DP700-1.4. For all MS steels, the reduction factor of 0.75 is applied. The upper limit of 414 MPa is ignored, as an AHSS bolted connection study using the same steels [30] has found the upper limit to be unnecessary.

The reduced yield stress leads to a large improvement of DSM performance (see Table 3). Compared to the classical DSM, Method 1 improves the overall mean test-to-predicted ratio from 0.89 to 0.99 and reduces COV from 0.16 to 0.15. The difference is largely driven by the large improvement of accuracy for the Sigma sections. However, the DSM predictions for Sigma sections are still unconservative overall. The difference in performance between C and Sigma sections, though reduced, still exists.

8.2 Method 2: Considering L-D buckling interactions + reduced yield stress

Buckling interactions have been suggested in the literature as one of the causes for reduced column buckling strengths. In this study, visual evidence of buckling interactions is observed during testing, which include interactions between local and distortional buckling (L-D) are not currently considered in the DSM. A companion study of this research program finds that adding L-D interaction limit state is effective in improving DSM accuracy for AHSS flexural members. [18]. It is natural to investigate if such approach can benefit compression members. The current DSM equations can be adapted for L-D limit state.

For L-D interaction limit state, the nominal buckling strength is calculated per Eq. (6)

$$P_{n\ell d} = \begin{cases} P_{nd} & \lambda_{\ell d} \leq 0.776 \\ (1 - 0.15\lambda_{\ell d}^{-0.8})\lambda_{\ell d}^{-0.8} P_{nd} & \lambda_{\ell d} > 0.776 \end{cases} \qquad \text{Eq. (6)}$$

where $\lambda_{\ell d} = \sqrt{P_{nd}/P_{cr\ell}}$

Considering L-D limit state and reduced F_y leads to acceptable DSM performance, with the test-to-predicted ratio being 1.07 and COV being 0.16. The overall accuracy is better than the classical DSM (see Table 3). Compared to Method 1 which only considers reduced F_y, the predictions for the Sigma sections are accurate. However, the predictions for the C sections are worse – the test-to-predicted ratio ballons from 1.08 to 1.21.

8.3 Recommended methods

Method 1 is an easily implemented approach that indirectly addresses the complexities (buckling interactions, cross-section differences, etc.) in an all-encompassing way. The reduction factors alone allow DSM to deliver accurate strength predictions for all C section columns. The drawback of Method 1 is its inconsistency over longer Sigma columns. Method 2, though more complex to implement, are more tailored approaches that directly address the nuances of buckling interactions, which may prove to be more effective if applied over a wider range of data. Overall, all two methods provide acceptable and beneficial improvement over the current form of DSM. However, the non-uniform performance of DSM over C and Sigma sections seems to suggest that signals beyond member slenderness (λ_ℓ, λ_d) exist and play a role in the compressive strengths of AHSS members. Further study is needed to uncover such signals relevant to AHSS members.

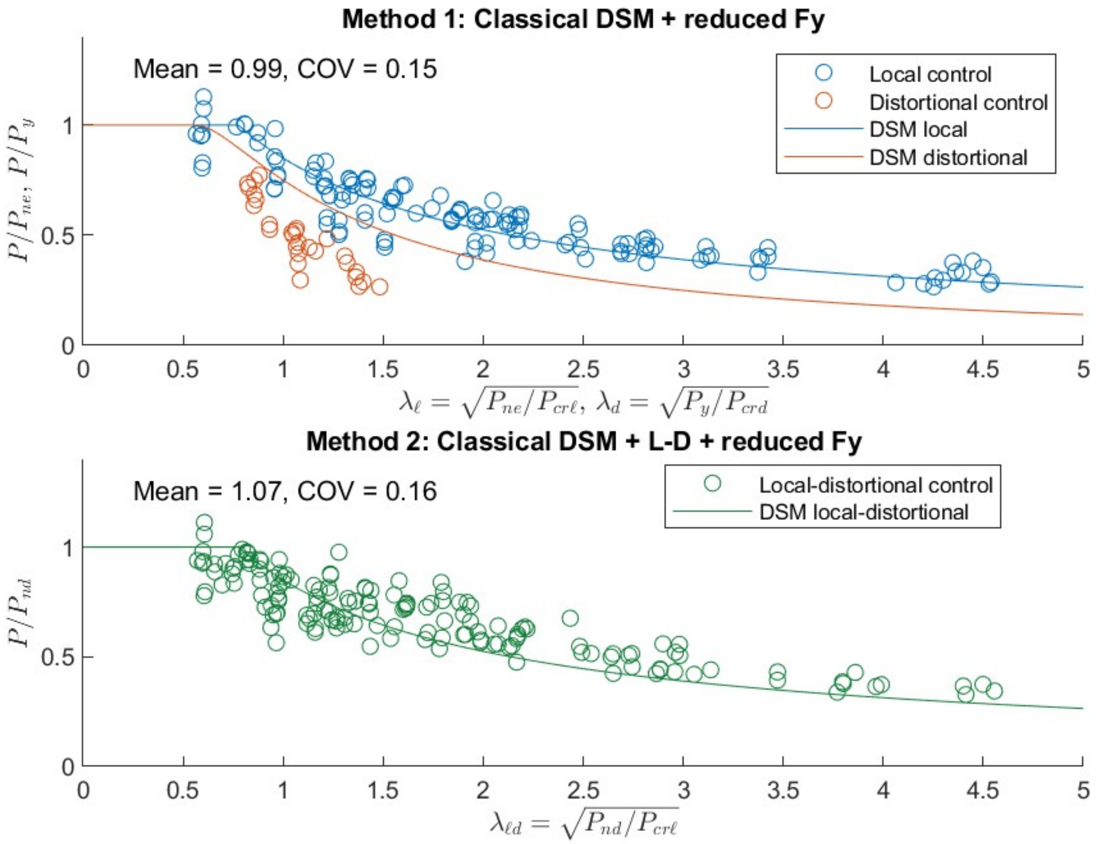

Fig. 20. Performance of the recommended methods

9. Conclusions

An experimental study has been conducted to investigate the compressive strengths of cold-formed steel columns made from advanced high strength steel (AHSS) sheets with nominal F_y up to 1200 MPa. The experiment results indicate that adopting AHSS can lead to large increases in member strengths (e.g., 3X mild steel equivalent column strengths for MS1200 at certain lengths). Several forms of buckling interactions are found to manifest in the failures of the column tests with higher steel yield stresses and longer member lengths (610 mm and 1209 mm). This study finds that the Direct Strength Method (DSM) in the AISI S100 cannot consistently provide conservative strength predictions for all subsets of column tests. To extend the applicability of the Direct Strength Method, three modifications are found that can lead to satisfactory predictions: (1) use reduced yield stress values based on material ductility, (2) add local-distortional interaction to the current design checks. All two extensions to the current DSM can produce reliable strength predictions for the columns tested in this study. Overall, this study examines the buckling behavior and strengths of cold-formed steel (CFS) compression members with ultra-high yield stresses for which there has only been limited experimental studies. The design method proposed herein will contribute to the adoption of this new generations of high-strength steel in CFS construction.

Appendix 1. Sensitivity analysis of FE contact models

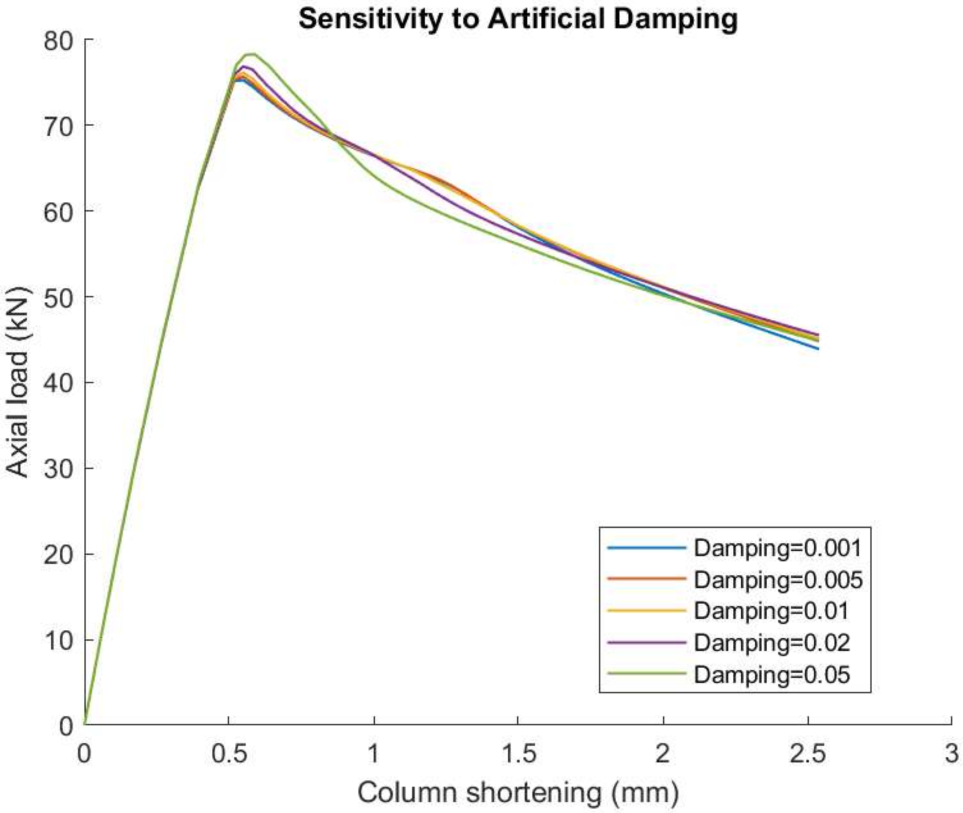

Fig. 21. Sensitivity analysis for artificial damping ratios on specimen 102C-340Fy-1.3t-610L

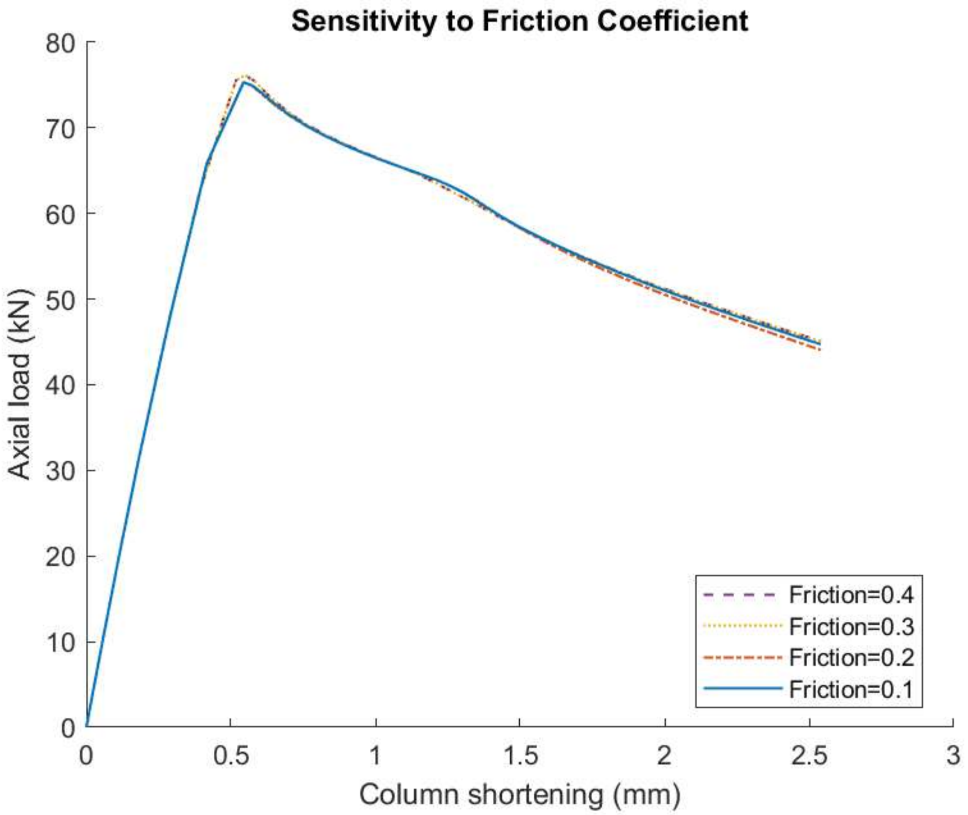

Fig. 22. Sensitivity analysis for contact friction coefficient on specimen 102C-340Fy-1.3t-610L

Appendix 2. Strength predictions of column specimens

Table 4. Elastic critical buckling loads under C-C and corresponding nominal buckling strengths by DSM

Name	P_u (kN)	P_y (kN)	P_{crl} (kN)	P_{crd} (kN)	P_{cre} (kN)	P_{ne} (kN)	P_{nlg} (kN)	P_{nd} (kN)	P_{nld} (kN)	P_{ndg} (kN)
305 mm columns										
102C-340Fy-1.3t-305L-1	77.6	104.7	51.2	552.8	3270.8	103.3	69.2	104.7	69.8	103.3
102C-340Fy-1.3t-305L-2	78.1	104.6	51.4	553.4	3242.4	103.2	69.3	104.6	69.9	103.2
102C-550Fy-1.2t-305L-1	91.7	182.6	38.8	536.8	2817.4	177.7	88.8	182.2	90.3	177.6
102C-700Fy*-1.4t-305L-1	138.1	231.6	63.7	608.8	3378.5	225.0	123.5	228.9	124.9	223.1
102C-700Fy-1.4t-305L-1	131.2	242.4	59.7	661.3	3268.0	235.0	124.0	240.6	125.9	233.9
102C-700Fy-1.4t-305L-2	130.4	243.5	60.0	585.6	3340.0	236.2	124.7	237.8	125.2	231.7
102C-1030Fy-1.0t-305L-1	92.8	267.2	24.6	356.8	2363.9	254.8	94.2	223.3	86.7	216.5
102C-1030Fy-1.0t-305L-2	94.1	266.9	24.3	355.8	2357.0	254.5	93.7	222.9	86.2	216.1
102C-1200Fy-1.4t-305L-1	191.5	447.3	67.3	690.7	3495.8	424.0	188.5	392.2	179.5	377.8
102C-1200Fy-1.4t-305L-2	188.1	448.3	67.5	688.5	3445.9	424.6	188.8	392.4	179.7	377.8
102C-1200Fy-2.0t-305L-1	345.1	665.2	188.0	1125.0	4799.5	627.7	351.7	599.4	341.4	574.8
102C-1200Fy-2.0t-305L-2	349.4	669.2	186.2	1124.9	4909.7	632.0	352.0	601.8	341.1	577.6
102Sigma-340Fy-1.3t-305L-1	118.8	112.2	305.4	626.6	3373.6	110.6	110.6	112.2	112.2	110.6
102Sigma-340Fy-1.3t-305L-2	124.6	112.0	304.8	628.6	3357.5	110.5	110.5	112.0	112.0	110.5
102Sigma-550Fy-1.2t-305L-1	163.6	202.5	233.6	535.1	3164.5	197.2	177.1	200.3	179.0	195.6
102Sigma-550Fy-1.2t-305L-2	171.6	202.5	233.6	535.1	3164.5	197.2	177.1	200.3	179.0	195.6
102Sigma-700Fy*-1.4t-305L-2	220.3	253.3	378.2	769.5	3662.7	246.1	240.2	253.2	244.9	246.1
102Sigma-700Fy-1.4t-305L-1	232.7	265.2	353.6	728.4	3596.8	257.1	242.3	263.4	246.3	256.0
102Sigma-700Fy-1.4t-305L-2	232.7	264.4	355.5	725.5	3546.4	256.2	242.1	262.5	246.2	255.1
102Sigma-1030Fy-1.0t-305L-1	175.3	292.1	156.3	609.3	2639.9	278.9	194.9	277.6	194.3	267.6
102Sigma-1030Fy-1.0t-305L-3	167.0	289.9	158.3	608.9	2610.3	276.7	194.8	275.9	194.4	266.0

102Sigma-1030Fy-1.0t-305L-4	161.8	291.5	159.0	611.5	2608.9	278.2	195.7	277.4	195.4	267.3
102Sigma-1200Fy-1.0t-305L-1	178.9	327.3	162.9	387.9	2762.4	311.4	212.5	262.1	189.8	253.9
102Sigma-1200Fy-1.0t-305L-2	167.4	319.8	157.7	623.3	2696.8	304.3	207.0	299.2	204.7	288.1
102Sigma-1200Fy-1.0t-305L-3	170.5	326.9	163.1	573.0	2759.0	311.1	212.4	297.5	206.3	286.9
102Sigma-1200Fy-1.0t-305L-4	193.5	320.5	157.8	622.7	2712.3	305.0	207.3	299.6	204.9	288.5
102Sigma-1200Fy-1.4t-305L-1	299.9	487.0	382.0	1352.2	3605.1	460.2	367.7	484.1	380.2	459.3
102Sigma-1200Fy-1.4t-305L-2	344.5	487.0	380.2	1353.9	3605.7	460.2	367.1	484.1	379.7	459.3
152C-340Fy-1.3t-305L-1	81.0	148.7	32.8	1460.9	6718.2	147.3	74.1	148.7	74.6	147.3
152C-340Fy-1.3t-305L-2	81.9	148.8	32.4	1462.2	6737.9	147.5	73.8	148.8	74.3	147.5
152C-550Fy-1.2t-305L-1	104.6	263.7	24.1	1235.5	6202.5	259.0	94.4	263.7	95.4	259.0
152C-700Fy*-1.4t-305L-1	137.1	335.3	40.1	1678.9	7269.3	328.9	132.5	335.3	134.1	328.9
152C-700Fy-1.4t-305L-1	133.2	349.4	38.3	1623.1	7120.1	342.3	133.6	349.4	135.3	342.3
152C-700Fy-1.4t-305L-2	139.1	350.8	37.9	1634.8	7100.1	343.6	133.5	350.8	135.2	343.6
152C-1030Fy-1.0t-305L-1	94.9	386.3	14.9	886.2	5081.7	374.2	98.7	374.2	98.7	364.5
152C-1030Fy-1.0t-305L-2	106.5	387.3	15.0	1124.2	5057.3	375.0	99.2	386.2	101.0	374.6
152C-1200Fy-1.0t-305L-1	107.8	417.7	15.1	1127.4	5143.1	403.7	104.1	414.1	105.7	401.5
152C-1200Fy-1.0t-305L-2	116.3	415.7	15.4	897.0	5060.7	401.6	104.4	397.9	103.8	387.1
152C-1200Fy-1.4t-305L-1	190.3	645.2	40.2	1694.4	7303.9	621.8	197.4	637.7	200.5	617.0
152C-1200Fy-1.4t-305L-2	208.9	646.2	40.2	1685.7	7224.7	622.5	197.6	638.2	200.7	617.3
152C-1200Fy-2.0t-305L-1	368.9	964.8	114.2	1781.5	10151.7	927.1	375.1	890.4	365.7	864.4
152C-1200Fy-2.0t-305L-2	388.4	967.1	115.1	1760.5	10238.4	929.6	376.9	889.2	366.5	863.6
152Sigma-340Fy-1.3t-305L-1	118.6	154.6	161.8	1437.4	6652.0	153.1	132.5	154.6	133.4	153.1
152Sigma-340Fy-1.3t-305L-2	118.4	156.3	163.6	1443.5	6676.4	154.8	134.0	156.3	134.9	154.8
152Sigma-550Fy-1.2t-305L-2	175.7	277.9	121.4	1219.2	5990.7	272.6	175.8	277.9	178.0	272.6
152Sigma-700Fy*-1.4t-305L-1	212.5	354.0	206.1	1432.5	7176.1	346.8	247.3	354.0	250.7	346.8
152Sigma-700Fy*-1.4t-305L-2	213.1	354.0	206.1	1432.5	7176.1	346.8	247.3	354.0	250.7	346.8
152Sigma-700Fy-1.4t-305L-1	216.8	372.1	195.9	1374.3	7067.3	364.0	250.8	372.1	254.5	364.0
152Sigma-700Fy-1.4t-305L-2	225.6	369.0	194.2	1614.9	7403.8	361.4	248.9	369.0	252.3	361.4
152Sigma-1030Fy-1.0t-305L-1	197.5	411.1	71.6	946.8	5111.2	397.5	185.1	398.5	185.4	387.5
152Sigma-1030Fy-1.0t-305L-2	173.1	412.7	71.9	1214.8	5200.3	399.2	185.9	411.9	189.6	398.9
152Sigma-1200Fy-1.0t-305L-1	188.3	442.7	84.0	1290.0	5231.0	427.3	205.4	441.6	209.8	426.9
152Sigma-1200Fy-1.0t-305L-2	190.8	441.7	83.8	1188.2	5215.2	426.3	205.0	437.7	208.4	423.9
152Sigma-1200Fy-1.4t-305L-1	299.8	689.0	217.4	1433.6	7477.3	662.9	383.7	654.4	380.5	634.9
152Sigma-1200Fy-1.4t-305L-2	322.1	677.5	208.8	1441.3	7178.4	651.3	373.9	646.6	372.1	626.6
610 mm columns										
102C-340Fy-1.3t-610L-1	71.6	104.5	51.4	182.8	1207.9	100.8	68.2	95.0	65.6	92.6
102C-340Fy-1.3t-610L-2	72.6	103.4	55.0	204.5	1186.7	99.7	69.3	97.1	68.1	94.4
102C-340Fy-1.3t-610L-3	74.0	103.3	55.2	201.5	1104.1	99.3	69.2	96.7	68.0	93.8
102C-550Fy-1.2t-610L-1	87.2	182.6	38.8	145.9	1056.4	169.9	86.3	124.7	70.9	119.7
102C-700Fy*-1.4t-610L-1	120.8	231.3	63.9	202.7	1243.0	214.0	119.7	164.3	101.0	157.0
102C-700Fy-1.4t-610L-1	114.3	243.3	59.9	195.6	1236.5	224.0	120.5	166.6	99.6	158.9
102C-700Fy-1.4t-610L-2	115.4	243.3	59.9	194.1	1234.3	224.0	120.5	166.1	99.4	158.4
102C-700Fy-1.4t-610L-3	116.7	244.1	59.8	194.5	1158.7	223.5	120.2	166.5	99.5	158.3
102C-1030Fy-1.0t-610L-1	76.8	268.1	25.4	124.4	955.9	238.4	91.4	142.5	66.1	134.1
102C-1030Fy-1.0t-610L-2	77.1	269.4	24.8	120.9	970.1	239.8	91.0	140.8	65.1	132.7
102C-1200Fy-1.4t-610L-1	179.0	449.4	66.6	226.6	1294.6	388.6	177.7	248.6	133.8	230.3
102C-1200Fy-1.4t-610L-2	155.9	449.9	63.8	210.2	1106.9	379.5	172.4	239.9	128.8	219.6
102C-1200Fy-1.4t-610L-3	166.2	450.9	64.3	214.9	1396.1	393.9	176.9	242.7	130.1	226.2
102C-1200Fy-2.0t-610L-1	299.9	668.4	185.8	481.4	1791.5	571.7	329.8	436.2	277.0	399.4
102C-1200Fy-2.0t-610L-2	300.8	670.7	185.5	474.7	1924.8	579.7	332.6	434.3	276.1	400.2
102C-1200Fy-2.0t-610L-3	295.4	668.4	184.9	303.8	1659.1	564.7	326.6	351.6	240.4	322.2
102Sigma-340Fy-1.3t-610L-1	108.2	111.7	308.3	293.0	1299.5	107.7	107.7	110.4	110.4	106.9
102Sigma-340Fy-1.3t-610L-2	103.3	111.9	304.9	293.0	1342.9	108.1	108.1	110.6	110.6	107.2
102Sigma-340Fy-1.3t-610L-3	102.1	111.6	309.2	289.6	1226.1	107.4	107.4	110.1	110.1	106.5
102Sigma-550Fy-1.2t-610L-1	149.2	199.1	238.1	243.7	1128.2	184.9	170.7	161.3	155.5	153.9
102Sigma-550Fy-1.2t-610L-2	147.1	200.6	233.7	267.2	1423.1	189.1	172.2	167.5	158.6	161.1
102Sigma-700Fy*-1.4t-610L-1	180.2	251.4	383.7	330.4	1403.4	233.3	232.6	209.0	209.0	198.9
102Sigma-700Fy-1.4t-610L-1	181.7	265.2	357.7	326.0	1403.1	245.0	235.3	215.2	215.2	204.5
102Sigma-700Fy-1.4t-610L-2	168.3	265.2	353.3	327.7	1433.0	245.4	234.7	215.6	214.7	205.1
102Sigma-700Fy-1.4t-610L-3	175.2	264.9	359.3	319.5	1317.4	243.5	234.7	213.5	213.5	202.3
102Sigma-1030Fy-1.0t-610L-1	131.4	292.7	156.5	193.3	1050.7	260.5	186.5	183.7	148.1	172.3

102Sigma-1030Fy-1.0t-610L-2	135.4	290.2	159.2	188.4	1033.0	258.0	186.4	180.7	147.3	169.4
102Sigma-1200Fy-1.0t-610L-1	142.3	320.5	157.9	188.5	1077.1	283.0	197.5	190.7	152.3	178.3
102Sigma-1200Fy-1.0t-610L-2	140.6	328.3	162.2	182.4	1116.0	290.2	202.6	190.2	153.3	178.1
102Sigma-1200Fy-1.4t-610L-1	249.8	488.6	380.7	336.2	1437.3	423.8	347.7	312.4	283.2	288.6
102Sigma-1200Fy-1.4t-610L-2	244.5	488.6	381.1	333.0	1439.5	423.9	347.8	311.1	282.5	287.4
102Sigma-1200Fy-1.4t-610L-3	252.9	487.0	383.5	324.0	1318.2	417.2	344.9	306.7	280.3	281.5
102Sigma-1200Fy-2.0t-610L-1	380.5	722.6	989.7	622.6	1973.3	619.9	612.3	509.7	509.7	465.7
102Sigma-1200Fy-2.0t-610L-2	396.8	724.1	997.2	625.8	1979.1	621.3	614.7	511.5	511.5	467.3
152C-340Fy-1.3t-610L-1	68.9	148.5	30.8	355.1	2781.1	145.2	71.8	144.8	71.7	142.1
152C-340Fy-1.3t-610L-2	84.7	148.5	30.9	361.5	2994.4	145.4	72.0	145.3	71.9	142.7
152C-550Fy-1.2t-610L-1	92.6	264.9	23.6	443.9	2789.1	254.6	92.7	238.1	88.9	231.4
152C-550Fy-1.2t-610L-2	88.4	263.2	23.9	320.6	2537.5	252.1	92.5	212.9	83.2	207.1
152C-700Fy*-1.4t-610L-1	132.8	334.5	40.0	432.5	3045.9	319.5	130.0	276.4	118.7	268.3
152C-700Fy-1.4t-610L-1	137.7	351.1	38.2	441.4	3185.0	335.3	131.8	287.3	119.6	278.8
152C-700Fy-1.4t-610L-2	113.7	350.5	38.2	442.2	3187.6	334.8	131.6	287.2	119.5	278.7
152C-700Fy-1.4t-610L-3	132.9	350.8	38.2	432.1	3029.4	334.2	131.5	284.9	119.0	276.2
152C-1030Fy-1.0t-610L-1	73.2	388.2	15.2	284.4	2154.6	360.0	97.3	255.3	78.6	244.7
152C-1030Fy-1.0t-610L-2	84.6	387.9	15.2	294.4	2285.3	361.3	97.4	259.1	79.3	248.9
152C-1030Fy-1.0t-610L-3	81.5	387.9	14.9	282.4	2284.6	361.3	96.8	254.4	77.9	244.4
152C-1200Fy-1.0t-610L-1	86.3	422.1	14.5	297.1	2380.2	391.9	100.7	272.7	80.5	261.6
152C-1200Fy-1.0t-610L-2	97.5	416.7	15.3	290.7	2299.6	386.2	101.7	268.1	81.2	257.0
152C-1200Fy-1.0t-610L-3	83.1	421.7	14.5	287.2	2213.7	389.4	100.3	268.4	79.7	256.9
152C-1200Fy-1.4t-610L-1	151.4	648.8	40.1	440.7	3119.9	594.7	191.9	412.4	152.7	393.1
152C-1200Fy-1.4t-610L-2	178.7	647.3	39.7	451.2	3275.0	595.9	191.5	416.3	153.1	397.6
152C-1200Fy-1.4t-610L-3	181.9	647.3	39.9	439.3	3081.3	592.8	191.1	411.3	152.2	391.8
152C-1200Fy-2.0t-610L-1	316.0	961.6	114.6	410.5	4606.4	881.2	363.8	490.4	251.2	469.1
152C-1200Fy-2.0t-610L-2	302.0	969.5	110.1	387.5	4674.2	888.9	360.4	478.6	243.7	458.1
152Sigma-340Fy-1.3t-610L-1	109.0	156.8	167.9	476.2	3229.9	153.6	134.5	156.7	136.2	153.6
152Sigma-340Fy-1.3t-610L-2	128.0	156.2	163.5	327.5	2968.5	152.8	132.8	148.6	130.3	146.0
152Sigma-340Fy-1.3t-610L-3	109.3	156.8	168.0	324.8	3032.2	153.4	134.3	148.8	131.6	146.3
152Sigma-550Fy-1.2t-610L-1	136.3	276.6	120.8	762.7	2754.8	265.2	172.5	274.8	176.5	264.4
152Sigma-550Fy-1.2t-610L-2	144.7	277.3	121.1	408.0	2765.5	265.9	172.9	239.4	161.5	232.6
152Sigma-700Fy*-1.4t-610L-1	168.0	353.5	205.8	389.2	3381.4	338.3	243.2	275.3	212.3	267.9
152Sigma-700Fy*-1.4t-610L-2	177.5	353.7	205.9	386.9	3393.0	338.6	243.4	274.8	212.1	267.5
152Sigma-700Fy-1.4t-610L-1	180.7	369.0	194.2	369.2	3163.6	351.4	244.4	276.8	209.0	268.8
152Sigma-700Fy-1.4t-610L-2	159.9	369.3	194.4	375.0	3127.5	351.4	244.5	278.7	209.9	270.4
152Sigma-700Fy-1.4t-610L-3	164.6	369.3	194.4	377.3	3340.1	352.6	245.0	279.3	210.3	271.6
152Sigma-1030Fy-1.0t-610L-2	121.5	409.5	71.3	293.9	2273.0	379.8	179.6	266.9	143.5	255.8
152Sigma-1030Fy-1.0t-610L-3	136.1	413.3	72.0	308.3	2307.8	383.5	181.3	273.9	146.4	262.6
152Sigma-1200Fy-1.0t-610L-1	138.0	443.7	81.6	298.1	2276.8	408.9	197.7	280.7	155.6	268.3
152Sigma-1200Fy-1.0t-610L-2	145.7	436.9	80.3	305.0	2306.2	403.6	195.0	281.2	154.9	269.1
152Sigma-1200Fy-1.0t-610L-3	173.4	440.3	81.0	301.6	2291.5	406.3	196.3	281.0	155.2	268.7
152Sigma-1200Fy-1.4t-610L-1	221.8	676.5	208.4	374.7	3095.8	617.4	361.0	391.4	268.7	372.8
152Sigma-1200Fy-1.4t-610L-2	211.4	677.0	208.6	374.2	3108.4	618.0	361.4	391.3	268.8	372.8
152Sigma-1200Fy-1.4t-610L-3	227.9	677.5	208.8	378.1	3125.1	618.8	361.8	393.3	269.8	374.8
152Sigma-1200Fy-2.0t-610L-1	372.7	1003.4	565.7	651.4	4556.8	915.0	661.5	624.9	513.9	594.1
152Sigma-1200Fy-2.0t-610L-2	418.6	1004.1	566.1	650.4	4625.1	916.9	662.6	624.7	514.0	594.4
152Sigma-1200Fy-2.0t-610L-3	296.4	999.4	563.4	635.6	4313.7	907.1	656.8	616.6	508.7	584.8
1219 mm columns										
102C-340Fy-1.3t-1219L-1	68.8	104.3	51.5	106.6	327.1	91.2	63.9	78.9	58.1	72.7
102C-340Fy-1.3t-1219L-2	68.8	103.8	51.3	105.7	324.0	90.8	63.6	78.4	57.8	72.2
102C-700Fy-1.4t-1219L-1	100.2	243.5	60.3	117.4	338.2	180.2	105.0	131.8	85.8	112.4
102C-1030Fy-1.0t-1219L-1	65.1	269.7	24.6	61.6	242.3	169.3	72.8	99.8	52.1	79.7
102C-1200Fy-1.0t-1219L-1	59.5	292.5	24.1	61.4	249.6	179.1	74.9	103.4	52.9	81.8
102C-1200Fy-1.4t-1219L-1	135.6	450.4	64.2	124.7	350.3	263.0	136.9	184.4	109.0	141.2
102C-1200Fy-2.0t-1219L-1	222.2	669.2	184.2	258.2	494.0	379.6	252.3	324.6	227.8	241.5
102Sigma-340Fy-1.3t-1219L-1	94.8	111.9	308.8	189.9	372.9	98.7	98.7	100.9	100.9	92.1
102Sigma-700Fy-1.4t-1219L-1	140.4	264.9	351.6	209.7	405.5	201.5	201.5	180.2	180.2	153.5
102Sigma-1030Fy-1.0t-1219L-1	91.7	295.2	152.5	119.0	314.6	199.3	154.9	146.4	126.1	119.4
102Sigma-1030Fy-1.0t-1219L-2	97.6	292.7	157.1	117.7	303.9	195.6	154.5	145.0	126.5	117.6
102Sigma-1200Fy-1.0t-1219L-1	94.7	328.3	151.9	125.7	336.0	218.1	164.2	158.6	132.9	128.5

102Sigma-1200Fy-1.0t-1219L-2	86.6	322.9	155.0	127.3	312.8	209.6	161.1	158.3	133.6	126.6
102Sigma-1200Fy-1.4t-1219L-1	199.4	491.7	381.1	215.6	409.1	297.3	274.0	254.1	246.1	194.6
102Sigma-1200Fy-2.0t-1219L-1	288.0	720.2	1012.5	434.4	548.7	415.8	415.8	433.6	433.6	317.3
102Sigma-1200Fy-2.0t-1219L-2	295.2	720.2	998.9	436.5	542.3	413.1	413.1	434.6	434.6	316.6
152C-340Fy-1.3t-1219L-1	77.8	148.6	31.0	151.4	879.9	138.5	69.9	112.3	61.1	107.6
152C-700Fy-1.4t-1219L-1	117.8	351.7	38.2	185.2	954.3	301.4	123.2	198.6	94.7	183.0
152C-1030Fy-1.0t-1219L-1	69.3	388.5	14.7	86.9	677.2	305.6	86.8	142.0	53.9	126.8
152C-1200Fy-1.0t-1219L-1	73.3	422.1	14.8	90.5	698.6	327.8	90.9	151.0	56.1	134.0
152C-1200Fy-1.4t-1219L-1	160.5	648.3	40.1	190.3	974.3	490.7	170.2	273.5	118.0	238.6
152C-1200Fy-2.0t-1219L-1	275.5	964.8	115.3	466.1	1362.3	717.3	320.4	522.8	262.2	446.9
152Sigma-340Fy-1.3t-1219L-1	120.6	156.1	163.4	201.2	1006.8	146.3	128.9	128.8	118.3	123.5
152Sigma-700Fy-1.4t-1219L-1	178.7	369.0	194.2	223.3	1064.1	319.1	229.5	222.5	180.8	205.6
152Sigma-1030Fy-1.0t-1219L-1	99.3	410.2	71.4	127.3	773.5	328.5	163.9	178.1	110.7	159.7
152Sigma-1200Fy-1.4t-1219L-1	178.8	672.9	207.3	229.4	1028.4	511.7	319.2	306.6	228.5	267.3
152Sigma-1200Fy-2.0t-1219L-1	376.3	1004.1	566.1	432.8	1466.3	753.9	582.4	514.6	451.3	443.5

Data Availability Statement

Some or all data, models, or code that support the findings of this study are available from the corresponding author upon reasonable request.

Acknowledgements

This paper is based on the work supported by the National Science Foundation under grant 1760953 as part of the project “Optimization and Application of Next Generation Steels in Construction”. The authors appreciate Fabco Machine Corp. for helping press braking AHSS sheets to test specimens.

Disclaimer

Notation

The following symbols are used in this paper

F_y = Yield stress (MPa)
F_u = Ultimate tensile stress (MPa)
L = Member length (mm)
P_{cre} = Critical buckling load (kN)
P_{crd} = Critical distortional buckling load (kN)
$P_{cr\ell}$ = Critical local buckling load (kN)
P_n = Nominal compressive strength (kN)
P_{ne} = Nominal global buckling load (kN)
P_{nd} = Nominal distortional buckling load (kN)
P_{nd}^* = Nominal distortional buckling load with reduced post-buckling strength reserve (kN)
$P_{n\ell g}$ = Nominal local-global buckling load (kN)
P_{ndg} = Nominal distortional-global buckling load (kN)
$P_{n\ell d}$ = Nominal local-distortional buckling load (kN)
t = Member plate thickness (mm)
λ_c = Global buckling slenderness
λ_d = Distortional buckling slenderness
λ_d^* = Distortional buckling slenderness with reduced post-buckling strength reserve
λ_{dg} = Distortional-global buckling slenderness
$\lambda_{\ell g}$ = Local-global buckling slenderness
$\lambda_{\ell d}$ = Local-distortional buckling slenderness

References

[1] S. Keeler, M. Kimchi, P. Mooney, Advanced High-Strength Steels Application Guidelines Version 6.0, WorldAutoSteel, 2017.

[2] AISI S100, North American Specification for the Design of Cold-Formed Steel Structural Members, American Iron and Steel Institute, Washington, DC, 2022.

[3] AS/NZS 4600, Australian/New Zealand Standard: Cold Formed Steel Structures, 2018.

[4] B.W. Schafer, Local, Distortional, and Euler Buckling of Thin-Walled Columns, Journal of Structural Engineering 128 (2002) 289–299. https://doi.org/10.1061/(ASCE)0733-9445(2002)128:3(289).

[5] D. Akchurin, S. Torabian, B.W. Schafer, High-strength cold-formed steel stiffened channel section: Axial compressive strength and initial geometric imperfections, Thin-Walled Structures 206 (2025) 112604. https://doi.org/10.1016/j.tws.2024.112604.

[6] M.-T. Chen, B. Young, A.D. Martins, D. Camotim, P.B. Dinis, Experimental investigation on cold-formed steel stiffened lipped channel columns undergoing local-distortional interaction, Thin-Walled Structures 150 (2020) 106682. https://doi.org/10.1016/j.tws.2020.106682.

[7] D. Yang, G.J. Hancock, Compression Tests of High Strength Steel Channel Columns with Interaction between Local and Distortional Buckling, Journal of Structural Engineering 130 (2004) 1954–1963. https://doi.org/10.1061/(ASCE)0733-9445(2004)130:12(1954).

[8] D.C.Y. Yap, G.J. Hancock, Experimental Study of Complex High-Strength Cold-Formed Cross-Shaped Steel Section, Journal of Structural Engineering 134 (2008) 1322–1333. https://doi.org/10.1061/(ASCE)0733-9445(2008)134:8(1322).

[9] D.C.Y. Yap, G.J. Hancock, Experimental Study of High-Strength Cold-Formed Stiffened-Web C-Sections in Compression, Journal of Structural Engineering 137 (2011) 162–172. https://doi.org/10.1061/(ASCE)ST.1943-541X.0000271.

[10] D. Camotim, P.B. Dinis, Coupled instabilities with distortional buckling in cold-formed steel lipped channel columns, Thin-Walled Structures 49 (2011) 562–575. https://doi.org/10.1016/j.tws.2010.09.003.

[11] A.D. Martins, P.B. Dinis, D. Camotim, P. Providência, On the relevance of local–distortional interaction effects in the behaviour and design of cold-formed steel columns, Computers & Structures 160 (2015) 57–89. https://doi.org/10.1016/j.compstruc.2015.08.003.

[12] A.D. Martins, P.B. Dinis, D. Camotim, On the influence of local-distortional interaction in the behaviour and design of cold-formed steel web-stiffened lipped channel columns, Thin-Walled Structures 101 (2016) 181–204. https://doi.org/10.1016/j.tws.2015.11.021.

[13] A.D. Martins, D. Camotim, P. Borges Dinis, On the direct strength design of cold-formed steel columns failing in local-distortional interactive modes, Thin-Walled Structures 120 (2017) 432–445. https://doi.org/10.1016/j.tws.2017.06.027.

[14] G.Y. Matsubara, E. de Miranda Batista, Local–distortional buckling mode of steel cold-formed columns: Generalized direct strength design approach, Thin-Walled Structures 183 (2023) 110356. https://doi.org/10.1016/j.tws.2022.110356.

[15] A.D. Martins, D. Camotim, P.B. Dinis, On the distortional-global interaction in cold-formed steel columns: Relevance, post-buckling behaviour, strength and DSM design, Journal of

Constructional Steel Research 145 (2018) 449–470. https://doi.org/10.1016/j.jcsr.2018.02.031.

[16] D. Cava, D. Camotim, P.B. Dinis, A. Madeo, Numerical investigation and direct strength design of cold-formed steel lipped channel columns experiencing local–distortional–global interaction, Thin-Walled Structures 105 (2016) 231–247. https://doi.org/10.1016/j.tws.2016.03.025.

[17] P.B. Dinis, D. Camotim, B. Young, E.M. Batista, CFS lipped channel columns affected by L-D-G interaction. Part II: Numerical simulations and design considerations, Computers & Structures 207 (2018) 200–218. https://doi.org/10.1016/j.compstruc.2017.03.017.

[18] C. Ding, Y. Xia, D. Akchurin, H.B. Blum, Z. Li, B.W. Schafer, Flexural strength of advanced high strength steel lipped channels, Thin-Walled Structures 218 (2026) 114112. https://doi.org/10.1016/j.tws.2025.114112.

[19] C. Ding, Y. Xia, Damir Akchurin, Z. Li, H.B. Blum, B.W. Schafer, Simulation of compressive strength of wall studs cold-formed from advanced high strength steels, in: Proceedings of the Annual Stability Conference, Denver, Colorado, 2022.

[20] C.D. Moen, B.W. Schafer, Experiments on cold-formed steel columns with holes, Thin-Walled Structures 46 (2008) 1164–1182. https://doi.org/10.1016/j.tws.2008.01.021.

[21] S. Torabian, G.S. Chobe, J.K. Crews, B.W. Schafer, Stub column response in light of local vs distortional buckling, in: Proceedings of the Annual Stability Conference, Atlanta, 2020: p. 10.

[22] Yu Xia, Chu Ding, Zhanjie Li, Benjamin W. Schafer, Hannah B. Blum, Numerical modeling of stress-strain relationships for advanced high strength steels, Journal of Constructional Steel Research 182 (2021) 106687. https://doi.org/10.1016/j.jcsr.2021.106687.

[23] C. Ding, Strength and behavior of advanced high strength steel structural components, Ph.D. Dissertation, Johns Hopkins University, 2022.

[24] B.W. Schafer, CUFSM 5.04–finite strip buckling analysis of thin-walled members, (2020).

[25] Z. Li, B.W. Schafer, Application of the finite strip method in cold-formed steel member design, Journal of Constructional Steel Research 66 (2010) 971–980. https://doi.org/10.1016/j.jcsr.2010.04.001.

[26] B.W. Schafer, T. Peköz, Computational modeling of cold-formed steel: characterizing geometric imperfections and residual stresses, Journal of Constructional Steel Research 47 (1998) 193–210. https://doi.org/10.1016/S0143-974X(98)00007-8.

[27] Z. Li, B.W. Schafer, Buckling analysis of cold-formed steel members with general boundary conditions using CUFSM: conventional and constrained finite strip methods, in: Proceedings of Twentieth International Specialty Conference on Cold-Formed Steel Structures, Saint Louis, Missouri, 2010: p. 15.

[28] B.W. Schafer, S. Ádány, Buckling analysis of cold-formed steel members using CUFSM: conventional and constrained finite strip methods, in: Proceedings of 18th International Specialty Conference on Cold-Formed Steel Structures, Orlando, Florida, 2006: p. 16.

[29] S. Ádány, B.W. Schafer, A full modal decomposition of thin-walled, single-branched open cross-section members via the constrained finite strip method, Journal of Constructional Steel Research 64 (2008) 12–29. https://doi.org/10.1016/j.jcsr.2007.04.004.

[30] C. Ding, Y. Xia, Z. Li, H.B. Blum, B.W. Schafer, Strength of Bolted Lap Shear Connections with Advanced High-Strength Steel Sheets, J. Struct. Eng. 150 (2024) 04023208. https://doi.org/10.1061/JSENDH.STENG-12470.